Aging-aware optimal power management control and component sizing of a fuel cell hybrid electric vehicle powertrain

Samuel Filgueira da Silva [a], Jony Javorski Eckert [b,*], Fabrício Leonardo Silva [a], Fernanda Cristina Corrêa [c], Ludmila C.A. Silva [a], André Valente Bueno [b], Franco Giuseppe Dedini [a]

[a] *Integrated Systems Laboratory, School of Mechanical Engineering - FEM University of Campinas - UNICAMP, Campinas, SP, Brazil*
[b] *Engines Laboratory, Mechanical Engineering Department - Federal University of Ceará, Fortaleza, CE, Brazil*
[c] *Department of Electrical Engineering, Federal Technological University of Paraná, UTFPR Monteiro Lobato Avenue, Jardim Carvalho Ponta Grossa, PR, Brazil*

ABSTRACT

The current study presents a comprehensive approach for optimizing the power distribution control and design of a Fuel Cell Hybrid Electric Vehicle (FCHEV) equipped with a Battery-Ultracapacitor Hybrid Energy Storage System (HESS) using a multi-objective evolutionary algorithm called interactive adaptive-weight genetic algorithm (i-AWGA). The method aims to maximize the vehicle's driving range and the lifetimes of the fuel cell stack and battery while minimizing hydrogen fuel consumption and HESS size. The energy management strategy involves fuzzy logic controllers to distribute the power demand between the fuel cell and HESS and between the battery and ultracapacitor pack. Under the combined standardized cycle in which the optimization was developed, the optimized FCHEV configuration achieved a driving range of 444 km, hydrogen consumption of 0.9009 kg/100 km. Furthermore, the optimal configuration demonstrated robustness in real-world driving conditions, exhibiting improved energy efficiency, driving autonomy, and power sources lifespan. A cost–benefit analysis was also carried out, in which the optimized configuration was evaluated in terms of cost of ownership, achieving 31.28 US$/km, which means the substantial reduction of up to 63.59% in the invested cost-to-autonomy ratio as compared against other electrified vehicle powertrain topologies. Overall, this study offers a promising approach for designing efficient, cost-effective, and environmentally friendly FCHEVs with improved performance and durability.

1. Introduction

Audacious air quality management goals have recently been pursued by international authorities due to the negative impacts atmospheric pollution has caused to human health, environment and global economics [1]. In the last few years, global agreements, which propose a set of sustainable policy initiatives and target net-zero emissions by mid-century, have been adopted by different countries worldwide (e.g., Paris Agreement [2,3] and the European Green Deal [4]). At the same time, long-term measures of energy security have been discussed and implemented since the growing of global energy demand is a current reality. In this sense, decarbonization of the road-based transportation is of extreme importance in this context of environmental concern as the sector corresponds to over 20% of the greenhouse gas emissions in the globe [5], consuming around 81 trillion megajoules (MJ) [6]. Hence, eco-friendly vehicles have gained attention from policy-makers. In fact, the shortage of fossil fuel-based energy

sources and the immediate need for green propulsion technologies have pushed several nations to consider the implementation of exacting regulations towards the banning sales of new internal combustion engine vehicles (ICEVs) in the next decades [7–9].

In this scenario, vehicle electrification emerges as a very attractive alternative to substitute petroleum-powered vehicles since fully electric vehicles (EVs) are characterized by free emissions, high energy efficiency and quiet operation mode [10]. Given this fact, governmental incentives towards electrically propelled road vehicle adoption – which include free charging stations, tax exemptions and EV sales mandates [11] – have been provided by different countries in recent times [12–14]. In addition, much progress has been made by the research community with regard to the development of component sizing and power distribution control strategies for different electrified powertrain topologies [15–17], showing their potential as a low-carbon technology.

---

* Corresponding author.
E-mail addresses: s263121@dac.unicamp.br (S.F. da Silva), javorski@fem.unicamp.br (J.J. Eckert), f208583@dac.unicamp.br (F.L. Silva), fernandacorrea@utfpr.edu.br (F.C. Corrêa), ludmila@fem.unicamp.br (L.C.A. Silva), bueno@ufc.br (A.V. Bueno), dedini@fem.unicamp.br (F.G. Dedini).

Nomenclature

BOL	Beginning of life
EHHV	Electric hydraulic hybrid vehicle
EM	Electric motor
EOL	End of life
EV	Electric vehicle
FC	Fuel cell
FCHEV	Fuel cell hybrid electric vehicle
FTP-75	Federal Test Procedure at urban driving
HESS	Hybrid energy storage systems
HWFET	Highway Fuel Economy Test
ICEV	Internal combustion engine vehicle
i-AWGA	Interactive adaptive-weight genetic algorithm
LOM	Largest of maximum
MOM	Middle of maximum
PEM	Proton exchange membrane
SOM	Smallest of maximum
US06	Supplemental Federal Test Procedure
A	Tafel slope
A_f	Vehicle frontal area [m^2]
b	Front axle to gravity center [m]
c	Rear axle to gravity center [m]
Cap	Ultracapacitor type
C_1	First selected chromosomes
C_2	Second selected chromosomes
C_D	Drag coefficient
C_{eq}	Equivalent capacitance (ultracapacitor pack) [F]
$C(\mathbf{X})$	Fuel cell hybrid electric vehicle powertrain design variables constrains
C_{fz}	Fuzzy logic control constraints
COR	Performance coefficient
C_t	The charging time [s]
Cl	The maximum number of cycles
D_R	Driving range [km]
D_z	The defuzzification method (Centroid, Bisector, MOM, LOM or SOM)
DoD	The depth of discharge [%]
E	Voltage source [V]
E_n	Nernst voltage [V]
E_{oc}	Open circuit voltage [V]
f_1	The first optimization criterion, the maximization of the drive range
f_2	The second optimization criterion, the minimization of the hybrid energy storage system
f_3	The third optimization criterion, the minimization of the hydrogen consumption
f_4	The fourth optimization criterion, the minimization of the power sources degradation
F	Faraday constant [As/mol]
$Ft(\mathbf{X})$	The adaptive-weight fitness
g	Gravitational acceleration [m/s^2]
h	Gravity center height [m]
H	The cycle number constant
H_{cons}	Hydrogen consumption [kg/100 km]
I^*	Low-frequency battery current [A]
I_0	Exchange current [A]
I_{bat}	Battery current [A]
I_c^a	The mean current in charge [A]

I_d	Discharging current [A]
I_d^a	The mean current in discharge [A]
I_d	Differential rotating inertia [kgm^2]
I_{fc}	Fuel cell current [A]
I_w	The wheel inertia [kgm^2]
I/O_j	Generic coordinate of the input–output membership functions
J_c	The required energy in the battery recharge [Ws]
k	Number of half cycles
K_c	Voltage constant at nominal condition of operation
L	Wheelbase [m]
L_{fc}	Fuel cell lifetime [h]
L_{PS}	Power source degradation factor
M	Vehicle total mass [kg]
M_{bat}	Battery mass [kg]
M_{cap}	Ultracapacitor pack mass [kg]
M_{HESS}	HESS mass [kg]
M_{ref}	Reference vehicle mass [kg]
M_{uc}	Mass of a single ultracapacitor module [kg]
Mt	Mutation Operator
$\mathbf{MF_{PS}}$	Vector of the design variables of the input/output membership functions (power split: front and rear drive systems)
$\mathbf{MF_{FH}}$	Vector of the design variables of the input/output membership functions (power split: fuel cell and HESS)
$\mathbf{MF_{HS}}$	Vector of the design variables of the input/output membership functions (HESS power split control)
n_1	Number of start-stop cycles per hour
n_2	Power transition times per hour
N	Number of cells
N_d	Differential gear ratio
P_{air}	Absolute supply pressure of air [atm]
P_{batt}	Requested power for the battery pack [W]
P_{cap}	Requested power for the ultracapacitor pack [W]
P_{fuel}	Absolute supply pressure of fuel [atm]
P_{H2}	Partial pressure (hydrogen) [atm]
P_{HESS}	Requested power for the HESS [W]
$P_p(\mathbf{X})$	Penalty value
P_{O2}	Partial pressure (oxygen) [atm]
P_{req}	Required power [W]
P_{size}	Population size
Q	Actual battery capacity [Ah]
Q_{BOL}	Battery capacity at the beginning of life [Ah]
Q_{EOL}	Battery capacity at the end of life [Ah]
Q_{ini}	Initial electric charge [C]
Q_{nom}	Nominal battery capacity [Ah]
Q_T	Actual electric charge [C]
r	Tires radius [m]
R	Ideal gas constant [J/molK]
R_{Ceq}	Equivalent resistance (ultracapacitor pack) [Ω]
R_{fc}	Fuel cell internal resistance [Ω]
R_x	Rolling resistance [N]
$\mathbf{RW_{PS}}$	Vector of rule weights for the power split between front and rear drive systems
$\mathbf{RW_{FH}}$	Vector of rule weights for the power split between fuel cell and HESS
$\mathbf{RW_{HS}}$	Vector of rule weights for the HESS power split control
S_E	The specific energy for lithium-ion batteries [Wh/kg]
$S_P(\mathbf{X})$	The selection probability
S_{reg}	State variable for ultracapacitor

SoC_B The battery state of charge [%]

SoH The battery state of health

t Simulation time [s]

t_1 Idling power condition time per hour

t_2 High power condition time per hour

T_{amb} The ambient temperature [K]

T_d Response time [s]

T_{EM} Electric motor torque [Nm]

T_{fc} Fuel cell operating temperature [K]

T_F Effective traction torque at front wheels [Nm]

T_{Pc} The remaining point of torque at the constant power phase [Nm]

T_R Effective traction torque at rear wheels [Nm]

T_{ref} The nominal reference temperature [K]

T_{req} Required torque at the traction wheels [Nm]

U_{H2} Rate of conversion (hydrogen)

U_{O2} Rate of conversion (oxygen)

V Actual vehicle speed [m/s]

V_{air} Flow rate of air [l/min]

V_{bat} Battery dynamic voltage [V]

V_c Target vehicle speed (driving cycle) [m/s]

V_{ch} The maximum voltage of battery pack [V]

V_{Ceq} Equivalent voltage (ultracapacitor pack) [V]

V_{drop} Fuel cell voltage drop [μV/h]

V_{fuel} Flow rate of fuel [l/min]

V_H Voltage for the drive systems [V]

V_{nom} Nominal battery voltage [V]

w Percentage of water vapor [%]

x Percentage of hydrogen in the fuel [%]

$\mathbf{X}$ Chromosome with all design variables for each solution

$\mathbf{X_1}$ First selected chromosome

$\mathbf{X_2}$ Second selected chromosome

$\mathbf{X_{cr}}$ New chromosome generated by crossover

$\mathbf{X_M}$ New mutated chromosomes

y Percentage of oxygen in the air [%]

z Number of moving electrons

ΔV Allowable voltage loss for each fuel cell [V]

λ_{chg} Voltage degradation rate for the power transition [μV/cycle]

λ_{idl} Voltage degradation rate for the idling power condition time [μV/h]

λ_{hgh} Voltage degradation rate for the high power condition time [μV/h]

λ_{ss} Voltage degradation rate for the number of start-stop cycles [μV/cycle]

γ_c The exponent coefficient for mean recharge current

γ_d The exponent coefficient for mean discharge current

ϵ Aging factor

η_c The AC–DC conversion efficiency

η_{EM} Electric motor efficiency

η_{invF} Inverter efficiency (front system)

η_{invR} Inverter efficiency (rear system)

η_d The differential efficiency

θ Road slope [rad]

ρ Air density [kg/m^3]

ψ The Arrhenius rate constant [kJ/mol]

ω_{maxe} Maximum electric motor speed [rad/s]

ω_{P_e} Equivalent electric motor speed [rad/s]

ω_{T_e} Electric motor speed at the constant torque phase [rad/s]

However, it is also worth pointing out that electrically propelled vehicles still present important limitations that have prevented this type of powertrain architecture to be totally immersed in the global market. These EV drawbacks are typically related to oversizing, long charging time and limited driving autonomy [18]. Furthermore, EVs cannot necessarily be considered zero-emission vehicles, once the carbon emissions, which come from the energy sources that provide the required electricity demand for charging stations, should be taken into account in a further well-to-wheel analysis [19].

Despite the gradual reduction of lithium-ion battery prices (from 1000 US\$/kWh to 227 US\$/kWh [20] in the last decade), the battery pack still consists of a relevant parcel of EV cost. Additionally, earlier replacement of batteries results in a higher environmental impact, which is associated with the need for disposal and battery manufacturing [21,22]. Due to this fact, battery degradation is another limitation that should be considered in the energy management control of electrified vehicles [23]. To address this issue, battery-ultracapacitor hybrid energy storage system (HESS) is considered an attractive option since ultracapacitors (UCs) can be used as peak power buffer units in order to reduce battery stress in aggressive driving profiles [16,24], while performing more effective braking energy regeneration at low ambient temperature conditions [25]. In this manner, scholars have developed optimization-based power distribution control strategies for HESS-based EVs with the concurrent focus on maximization of battery lifespan and energy efficiency [26–28].

In this context, fuel cell hybrid electric vehicles (FCHEVs), which combine fuel cell stack and battery, outperform EVs regarding refueling time and driving range. Among the available types of fuel cell systems, the proton exchange membrane fuel cell (PEMFC) is currently the most used one in the automotive industry due to its lower operating temperature, high power density and more advanced technical maturity [29,30]. However, economic viability is currently one of the biggest challenges of such systems [31].

Although hydrogen-powered FCHEVs are still in the early stages of implementation, this propulsion technology has been considered one of the most promising and sustainable solutions to accomplish stringent road transport emission targets that have been planned for the next decades. This is due to the fact that PEM-based FCHEVs emit zero air pollutants and greenhouse gases from the exhaust system, with only water and warm air as byproducts of the fuel cell's chemical reaction [32]. Fuel cells also provide higher energy efficiency than conventional internal combustion engines, featuring no moving parts. The hydrogen, on the other hand, presents higher energy density per mass than petroleum-based fuels, but much lower volumetric energy, which requires the gas to be pressurized to 35–70 MPa in storage tanks [33]. Another important factor that should be highlighted is that green hydrogen production (when the fuel is obtained by water electrolysis using renewable energy sources) consists of one of the cleanest energy-conversion technologies to date [34] and is expected to be feasible for large-scale applications in the future, which may effectively contribute to economic growth in a more sustainable society [35,36]. In this sense, advances in fuel cell technology have currently been pursued by different automotive manufacturers such as Honda [37], Toyota [38,39], Hyundai [40], Nissan [41,42], BMW [43], Mercedes-Benz [44,45] etc.

In the academic field, scholars have conducted in-depth research on the optimality of fuel cell hybrid electric propulsion architectures with respect to the minimization of hydrogen fuel consumption [46–49], overall operating costs [46,50,51], and power sources degradation [52–54]. Published works have also investigated fuel cell-battery-ultracapacitor hybrid systems for vehicle powertrain design. In the study of Hu et al. [55], a battery aging-aware HESS optimization for a fuel cell hybrid electric bus configuration was employed, comparing the economical scenarios according to different battery sizes and replacement strategies. In the study of Wang et al. [56], the energy management control for a fuel cell-battery hybrid bus was optimized

to concurrently minimize hydrogen consumption and maximize the lifetime of electrochemical power sources, resulting in lower long-term operating costs. In a different approach, Khan et al. [57] implemented a backstepping sliding mode controller to obtain a reliable and stable fuel cell-ultracapacitor-based hybrid electric propulsion system. Moreover, Rahman et al. [58] developed a fuzzy logic based power management strategy for a FCHEV topology equipped with a battery-supercapacitor HESS, designing a supertwisting sliding mode-based controller to track the DC bus voltage reference value. In their work, the hydrogen consumption was reduced by 29% when compared to other FCHEVs available in the literature. Li et al. [52] employ an equivalent hydrogen consumption minimization strategy for a FCHEV that considers state of health of fuel cell and battery, validating the developed method through a built test bench. Fletcher et al. [53] develop an optimal energy management control strategy using stochastic dynamic programming, so that operating costs (hydrogen consumption and fuel cell degradation) could be minimized.

Although the fuel cell as the main power source can provide extended driving autonomy and carbon neutrality, it lacks fast dynamic response in driving profiles that require high power demand [59]. Ultracapacitors, on the other hand, have been widely used as an auxiliary energy storage system to perform in these driving conditions due to its high power density. At the same time, the battery plays an important role when high energy density is needed. Hence, a vehicle powertrain architecture that comprises both fuel cell system and battery-ultracapacitor HESS can be a promising alternative for the mobility sector, as it combines essential characteristics of a clean and sustainable transportation. Therefore, this work provides the optimization of the combined fuel cell, battery and UC power sources, aiming to enhance the vehicle driving range, dynamical response and overall energy efficiency. Nevertheless, it is worthy pointing out that the energy management control, which is responsible for managing the amount of hydrogen used by the fuel cell stack and the discharge rate of the battery and UC, is fundamental to ensure that the FCHEV operates efficiently, while taking into account the life cycle of the power sources. The powertrain design is likewise critical, since a suitable component sizing can reduce equivalent fuel consumption and energy consumption. The proposed FCHEV topology is illustrated by Fig. 1.

According to the extensive literature review performed for this work, there is still a research gap regarding concurrent optimization design and energy management control of PEM-based FCHEVs equipped with battery/UC HESS in order to simultaneously address the minimization of hydrogen consumption, system size, battery and fuel cell degradation, and maximization of driving autonomy. Hence, the main purpose of this work is to fulfill this specific gap by employing the Interactive-Weight Genetic Algorithm (i-AWGA) procedure, which optimizes several powertrain design variables and fuzzy logic controllers' parameters.

The manuscript is organized as follows: Section 2 introduces the vehicle model and its respective subsystems; Section 3 presents the fuzzy logic controllers that were used for the energy management; Section 4 describes the formulation of the optimization problem as well as the way how it was solved (i-AWGA method); In Section 5, the optimization results are discussed, and the optimal solutions analyzed; Section 6 presents the main conclusions.

2. Simulation model

The simulation model is based on the equations presented by Gillespie [60], with the required adaptations to fit the 4-wheel electric drive FCHEV drivetrain as presented previously by Eckert et al. [61]. Therefore, the required traction torque T_{req} [Nm] is calculated by Eq. (1) as a function of the vehicle speed V [m/s], mass M [kg], air density ρ [kg/m^3], vehicle frontal area A_f [m^2], drag coefficient C_D, gravitational acceleration g [m/s^2] and tire radius r [m].

$$T_{req} = \left(M \left(a_{req} + 0.01g \left(1 + \frac{2.24\, V}{100\ [\text{m/s}]} \right) \right) + \frac{1}{2} \rho V^2 C_D\, A_f \right) r \tag{1}$$

The required vehicle acceleration a_{req} [m^2] is given by Eq. (2), based on a target speed V_c [m/s] provided by the standard driving cycles, considering a time step Δ_t [s] ahead of the current simulation time, which is compared to the current vehicle speed V.

$$a_{req}(t) = \frac{V_c(t + \Delta_t) - V(t)}{\Delta_t} \tag{2}$$

In order to obtain robust optimized FCHEV configurations under different distinct driving conditions, this paper considers the combination of the FTP-75 (urban), HWFET (highway) and US06 (high power demand) driving cycles, in which the speed profiles are presented in Fig. 2.

Once the analyzed FCHEV presents two independent driving systems, (Fig. 1), the torque demand T_{req} is divided between the frontal and rear traction systems, by means of a power management control (discussed in detail in Section 3) that defines $0 \leq P_S \leq 1$ the value applied in Eqs. (3) and (4) to define the required torque for the frontal T_{reqF} [Nm] and rear T_{reqR} [Nm] EMs.

$$T_{reqF} = \frac{P_S T_{req} + I_{wf} \frac{a_{req}}{r}}{2} \tag{3}$$

$$T_{reqR} = \frac{(1 - P_S)T_{req} + \left(I_d N_d^2 + I_{wr} \right) \frac{a_{req}}{r}}{N_d \eta_d} \tag{4}$$
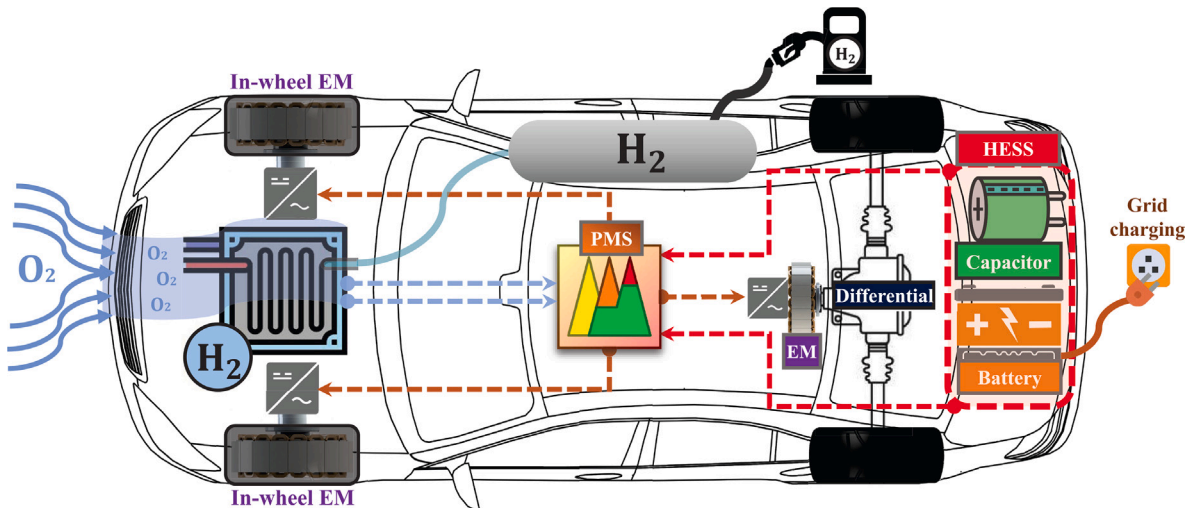

Fig. 1. FCHEV configuration.

(a) FTP-75
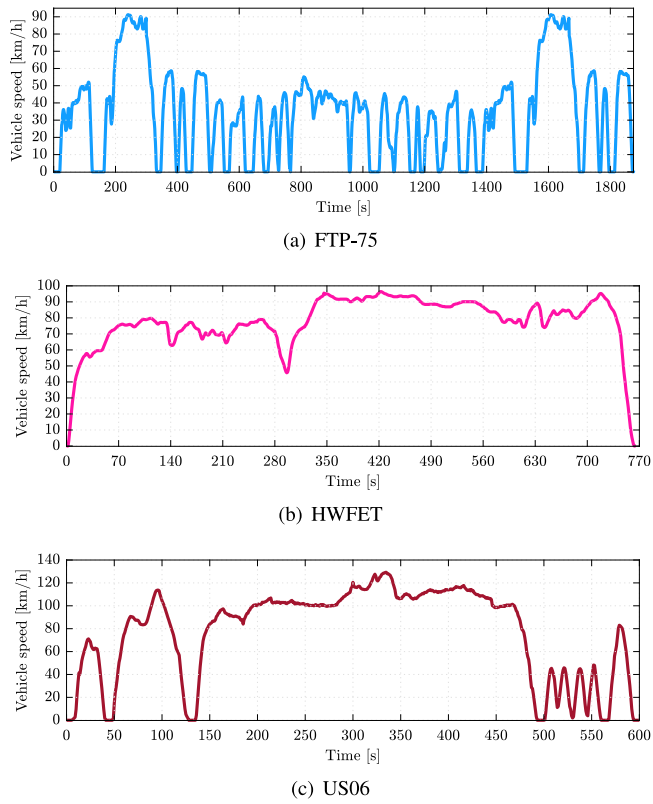

(b) HWFET

(c) US06

Fig. 2. Simulated driving cycles.

where, I_{wf} and I_{wR} [kgm^2] are the inertia of frontal and rear wheels, considering the addition of the respective EMs in case of in wheel EMs. The differential system transmission ratio N_d, mechanical efficiency η_d and equivalent inertia I_d [kgm^2].

However, the required torque cannot always be fulfilled by the respective EMs due to its torque curve limitations, that will be discussed in Section 2.2. Therefore, each EM has its maximum available torque T_{AF} and T_{AR} considering the frontal and rear systems.

Moreover, the traction torque applied in the tire ground contact at the frontal $T_{F(max)}$ [Nm] and rear $T_{R(max)}$ [Nm] also limited according to Eqs. (5) and (6) which defined the transmissible torque as a function of the tire ground friction coefficient μ, the vehicle gravity center height h [m], wheelbase L [m] and the distance between the gravity center and the frontal b [m] and rear c [m] axes.

$$T_{F(max)} = \mu \left(\frac{M g \ c}{2L} - \frac{M h \ a_x}{2L} \right) r \tag{5}$$

$$T_{R(max)} = \mu \left(\frac{M g \ b}{2L} + \frac{M h \ a_x}{2L} \right) r \tag{6}$$

Therefore, the effective traction torques at frontal T_F [Nm] and rear T_R [Nm] wheels are defined according to the rules presented in Eqs. (7) and (8).

$$T_F = \min \begin{cases} 2T_{EMF} - I_{wf} \frac{a_x}{r} \\ \\ 2T_{AF} - I_{wf} \frac{a_x}{r} \\ \\ T_{F(max)} \end{cases} \tag{7}$$

$$T_R = \min \begin{cases} T_{EMR} N_d \eta_d - \left(I_d N_d^2 + I_{wr} \right) \frac{a_x}{r} \\ \\ T_{AR} N_d \eta_d - \left(I_d N_d^2 + I_{wr} \right) \frac{a_x}{r} \\ \\ T_{R(max)} \end{cases} \tag{8}$$

Once, the effective torques are defined, it is possible to define the real vehicle acceleration a_x [m/s^2] by Eq. (9). As can be noticed, a_x changes the torque constrains (see Eqs. (5) to (8)), therefore, it is required an iterative process to reach the a_x convergence.

$$a_x = \frac{T_F + T_R}{Mr} - \frac{\rho V^2 C_D \ A_f + R_x}{2M} - 0.01g \left(1 + \frac{2.24 \ V}{100 \ [m/s]} \right) \tag{9}$$

After a_x convergence, the acceleration is integrated by ODE5 integrator from Simulink™ database to define the vehicle speed V and displacement. Finally, the torques applied effectively in the frontal T_{Fef} [Nm] and rear T_{Ref} [Nm] EMs are calculated by Eqs. (10) and (11).

$$T_{Fef} = \frac{T_F + I_{wf} \frac{a_x}{r}}{2} \tag{10}$$

$$T_{Ref} = \frac{T_R + \left(I_d N_d^2 + I_{wr} \right) \frac{a_x}{r}}{N_d \eta_d} \tag{11}$$

Table 1 shows the vehicle parameters applied in the current study. In the next subsections, design parameters from the energy storage systems are presented and they are optimized according to their respective constraints, as described by Section 4.2.

Table 1
Vehicle parameters [61,62].

Vehicle mass without HESS and fuel cell	800 kg
Tires 175/70 R13 radius (r)	0.2876 m
Wheels + tires inertia (I_w)	2 kgm^2
Tire peak friction coefficient (μ)	0.9
Vehicle frontal area (A)	1.8 m^2
Drag coefficient (C_D)	0.33
Differential efficiency (η_{td})	0.9
Wheelbase (L)	2.443 m
Gravity center height (h)	0.53 m
Front axle to gravity center (b)	0.983 m
Rear axle to gravity center (c)	1.460 m

2.1. Power source topology

In this work, DC-DC converters are used to connect the fuel cell stack (FC), battery, and ultracapacitor to the drive system [63]. The latter was introduced into the HESS (from now on, in this manuscript, HESS stands for the combination of battery and ultracapacitor) as the adoption of ultracapacitors can substantially reduce the life cycle cost of the system [64]. The FC-HESS topology features a parallel configuration, as depicted in Fig. 3. The advantage of this topology stems from
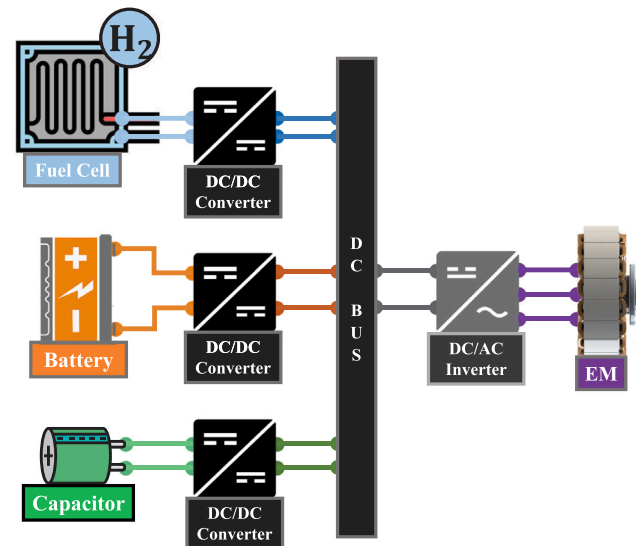

Fig. 3. Topology of the FC-HESS.

the fact that it can provide high precision for the power distribution between the sources, while offering high stability during operation with smooth electric current flow [65]. In the proposed configuration, the boost converters are employed to the battery and FC, and a buck-boost one is used for the ultracapacitor. That is, the negative power flow only occurs in the ultracapacitor, since it presents high power density. The buck-boost converter acts as a boost during discharge and as a buck for undercharging [66].

2.2. Electric motor model

In this study, a generic electric motor curve is used as a reference for the optimization design of front in-wheel and rear EMs considered in the FCHEV topology. As illustrated by Fig. 4a, four operating points define the EM torque curve, where T_{Pc} [Nm] (Eq. (12)), ω_{Pc} [rad/s] (Eq. (13)) are the torque and speed at constant power phase, respectively. The maximum EM speed at constant torque phase ω_{Tc} [rad/s], on the other hand, occurs at maximum torque T_{max} [Nm]. Lastly, the maximum EM speed ω_{max} [rad/s] is determined by linear progression according to the torque curve points previously mentioned. The presented method has successfully been applied in previous works [62,67] and is based on available database from the literature [68] along with experimental tests carried out by Yamashita et al. [69].

$$T_{Pc} = 0.3T_{max} \tag{12}$$

$$\omega_{Pc} = \frac{T_{max}\omega_{Tc}}{T_{Pc}} \tag{13}$$

The electric motors' ($\eta_{EM(F/R)}$), inverter' (η_{inv}) and DC bus (η_{DC}) efficiencies are also considered calculating the electric current required by the front I_F [A] (Eq. (14)) and rear drive I_R [A] (Eq. (15)) systems, where V_H [V] corresponds to the actual voltage of the drive system.

$$I_F = \frac{2T_{Fef}V}{r\,V_H\,\eta_{EMF}\,\eta_{invF}\,\eta_{DC}} \tag{14}$$

$$I_R = \frac{T_{Ref}V N_d}{r\,V_H\,\eta_{EMR}\,\eta_{invR}\,\eta_{DC}} \tag{15}$$

Hence, the required electrical power P_{req} [W] can be determined by Eq. (16).

$$P_{req} = (I_F + I_R)V_H \tag{16}$$

2.3. Battery model

In this study, the battery model is based on the Simulink™ battery block. The battery state of charge SoC_B is one of the fuzzy inputs in the HESS battery-ultracapacitor power split (see Section 3.2) and can be defined by Eq. (17), where Q [Ah] is the actual battery capacity and I_{batt} [A] represents the battery current. To avoid deep discharges that may negatively impact on the battery lifetime, the SoC_B is limited by the value of 40% [70,71], that is, 60% of depth of discharge DoD (Eq. (18)). With respect to the system mass M_{batt} [kg], it is calculated by Eq. (19), as a function of the lithium-ion battery energy density ($S_E = 150$ [Wh/kg] [72,73]), the rated voltage V_{nom} [V] and nominal capacity Q_{nom} [Ah].

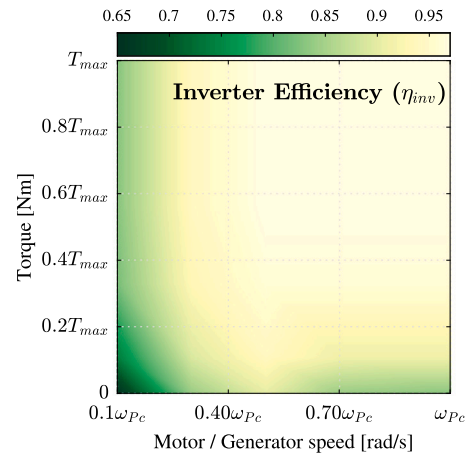$$SoC_B(t) = SoC_B(t_0) - \left(\frac{1}{Q(3600)}\int_0^t I_{batt}(\tau)d\tau\right) \times 100 \tag{17}$$

$$DoD(t) = 100 - SoC_B(t) \tag{18}$$

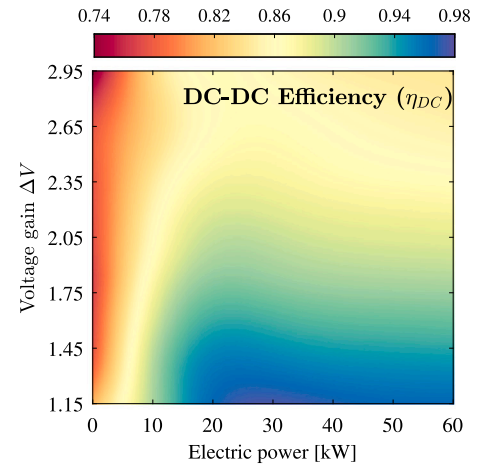$$M_{batt} = \frac{V_{nom}Q_{nom}}{S_E} \tag{19}$$

After the FCHEV model is subjected to the driving profile described previously in this section, the battery recharging is subsequently simulated, in which the final battery state of charge SoC_{Bfinal} is considered
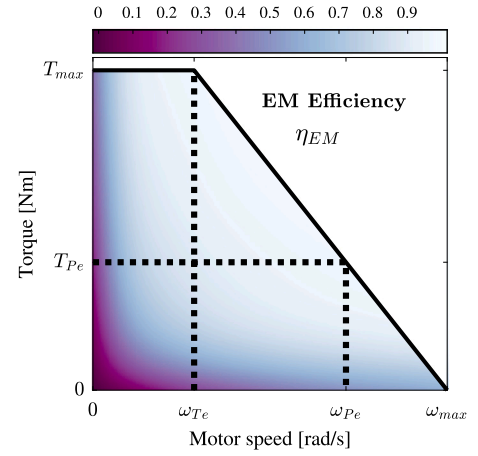
(a) Electric motors

(b) Inverter

(c) DC-DC converter

Fig. 4. Electric motors, inverter and DC-DC converter efficiency maps.

as the initial condition of the charging process. In this study, the charging current I_c [A] is set as constant to minimize the computational cost of the optimization procedure. For that, the constant value of I_c is defined based on the maximum battery voltage V_{ch} [V]. In addition, an efficiency η_c that encompasses both heat and AC–DC conversion losses is considered. Hence, the recharging energy J_c [J] is given by Eq. (20)

as a function of the recharging time C_t [s].

$$J_c = \int_0^{C_t} \eta_c I_c V_{ch} dt \qquad (20)$$

Moreover, the battery degradation is taken into account for the optimal design and power management control of the FCHEV powertrain, so that overloading can be avoided. In this work, the capacity fade model, proposed by Motapon et al. [74], presents a generic approach that has accurately been used to emulate the life cycle behavior of different types of lithium-ion batteries. For this current simulation, the ambient temperature T_{amb} was set as 293.15 K, in which temperature effects on the battery lifetime were neglected. The ultracapacitor degradation was likewise disregarded, since its lifespan is estimated to be greater than that of the vehicle itself [52,75].

The actual battery capacity Q [Ah] along the kth half cycle is calculated by Eq. (21), where Q_{BOL} and Q_{EOL} represent the capacity at the beginning of life (BOL) and end of life (EOL), respectively. In this case, the battery BOL refers to the initial condition of the battery's operational lifetime, in which the system is at its rated capacity, presents optimal performance and delivers full potential according to the manufacturer specification data. The battery EOL, on the other hand, corresponds to the final stage of the cycle life (generally 80% of the initial rated capacity), where the system is no longer able to provide the requested power, exhibiting lower energy capacity and higher internal resistance. In addition, the degradation factor ϵ, which varies from zero (BOL) to one (EOL) along the cycling, is determined by Eq. (22), as a function of the depth of discharge DoD. The maximum number of cycles Cl, on the other hand, is given by Eq. (23), in which H represents the cycle number constant, T_{ref} [K] denotes the nominal ambient temperature, ψ stands for the Arrhenius rate constant, I_c [A] corresponds to the average current for the half-cycle in charging mode, I_d [A] the average current for the half-cycle in discharging mode, ξ the exponent factor for DoD, γ_d the exponent factor for discharge current and γ_c the exponent factor for the charge current.

$$Q(k) = Q_{BOL} - \epsilon(k)(Q_{BOL} - Q_{EOL}) \qquad (21)$$

$$\epsilon(k) = \epsilon(k-1) + \frac{1}{2Cl(k-1)}\left(2 - \frac{DoD(k-2) + DoD(k)}{DoD(k-1)}\right) \qquad (22)$$

$$Cl(k) = H\left(\frac{DoD(k)}{100}\right)^{-\xi} \times$$
$$exp\left(-\psi\left(\frac{1}{T_{ref}} - \frac{1}{T_{amb}(k)}\right)\right)(I_d^a(k))^{-\gamma_d}(I_c^a(k))^{-\gamma_c} \qquad (23)$$

In this study, a battery state of health SoH indicator is used to present the actual working condition of the energy storage system. The ISO standard 12405 [76], which states that the battery reaches the end of its lifespan when the capacity is reduced to 80% of its original value, is used as a reference to estimate the state of health, expressed by Eq. (24), in which $SoH(k) \in [0.8, 1]$. For the optimization procedure, each battery configuration is subjected to a 3000-h cycling process, so that the capacity fade can be properly evaluated.

$$SoH(k) = \frac{Q(k)}{Q_{BOL}} \qquad (24)$$

It is also worth pointing out that, for this presented mathematical model, the first half cycle ($k = 1$) at the BOL stage is defined as a battery discharge. Once k reaches a value greater than 3 (that is, from fourth half-cycle onwards), the model can then determine the degradation factor ϵ, based on Eq. (22). Furthermore, such battery degradation model only takes into account cycle aging, disregarding capacity fade due to inactive time.

2.4. Ultracapacitor model

In this work, a generic model for ultracapacitors (UCs) is implemented, using the specification data of sixteen ultracapacitor configurations $Cap(n)$ that are available in the market, as presented by Table 2. The UCs can be arranged in series only, parallel only or the combination of series and parallel, depending upon the optimal search that is carried out by evolutionary algorithm, described in Section 4. Moreover, the optimization method tunes the number of ultracapacitors used in series N_s and in parallel N_p per branch. Once such parameters are defined, the overall mass of the ultracapacitor pack M_{cap} [kg] (Eq. (25)) can be calculated, where $M_{uc(n)}$ [kg] represents the mass of the ultracapacitor selected among those in Table 2. As a result, the total mass of the HESS M_{HESS} [kg] can be given by Eq. (26).

$$M_{cap} = N_s N_p M_{uc(n)} \qquad (25)$$

$$M_{HESS} = M_{bat} + M_{cap} \qquad (26)$$

Since the ultracapacitors are associated, the equivalent voltage V_{Ceq} [V], equivalent capacitance C_{eq} [F] and equivalent resistance R_{Ceq} [Ω] are given by Eq. (27), Eq. (28), and Eq. (29), respectively. Furthermore, the ultracapacitor state of charge SoC_C is calculated by Eq. (30), as a function of the current I_{cap} [A], initial electric charge Q_{ini} [C], and actual electric charge Q_T [C].

$$V_{Ceq} = \sum_{i=1}^{N_s} V_{Ci} \qquad (27)$$

$$C_{eq} = \sum_{k=1}^{N_p}\left(\frac{1}{\sum_{i=1}^{N_s}\frac{1}{C_i}}\right)_k \qquad (28)$$

$$R_{Ceq} = \left(\sum_{k=1}^{N_p}\left(\frac{1}{\sum_{i=1}^{N_s} R_i}\right)_k\right)^{-1} \qquad (29)$$

$$SoC_C(t) = \left(\frac{Q_{ini} - \int_0^t I_{cap}(\tau)d\tau}{Q_T}\right) \times 100 \qquad (30)$$

2.5. Fuel cell model

With regard to the PEM fuel cell simulation, the model was based on fuel cell stack governing equations, which emulate the nonlinear behavior of the system according to an equivalent circuit, as proposed by the literature [77,78]. For this model, the gases are assumed to be ideal, and electrode temperature maintains stable and equal to that of the stack. The voltage source E [V] is given by Eq. (31), in which N,

Table 2
Ultracapacitor parameters [61].

$Cap(n)$	$V_{uc(n)}$ [V]	$C_{uc(n)}$ [F]	$R_{uc(n)}$ [Ω]	$M_{uc(n)}$ [kg]
$Cap(1)$		108	3.6E−03	3.0
$Cap(2)$		108	4.3E−03	3.7
$Cap(3)$		200	3.5E−03	4.1
$Cap(4)$	6	266	3.0E−03	4.6
$Cap(5)$		333	2.4E−03	5.1
$Cap(6)$		500	1.9E−03	6.0
$Cap(7)$		36	13E−03	9.5
$Cap(8)$		66	10.4E−03	11.5
$Cap(9)$	48	88	8.9E−03	12.5
$Cap(10)$		111	7.1E−03	13.5
$Cap(11)$		166	5.6E−03	16.0
$Cap(12)$	64	83	9.5E−03	17.0
$Cap(13)$		125	7.5E−03	20.0
$Cap(14)$	86	62	12.7E−03	21.0
$Cap(15)$		93	10E−03	26.0
$Cap(16)$	125	62	15E−03	67.0

A, I_{fc} [A], I_0 [A] and T_d [s] represent the number of cells, Tafel slope, fuel cell current, exchange current and response time, respectively. Additionally, the open circuit voltage E_{oc} [V] can be calculated as a function of the Nernst voltage E_n [V] and the voltage constant at nominal condition of operation K_c, as shown in Eq. (32). The fuel cell voltage V_{fc} [V], on the other hand, is defined by Eq. (33), where R_{fc} [Ω] denotes the internal resistance.

$$E = E_{oc} - N A \ln \left(\frac{I_{fc}}{I_0} \right) \frac{1}{s T_d / 3 + 1} \tag{31}$$

$$E_{oc} = K_c E_n \tag{32}$$

$$V_{fc} = E - R_{fc} I_{fc} \tag{33}$$

The use of hydrogen and oxygen from the PEMFC can be represented by the rates of conversion U_{H2} (Eq. (34)) and U_{O2} (Eq. (35)), where R [J/molK] is the ideal gas constant, T_{fc} [K] denotes the operating temperature, z corresponds to the number of moving electrons, F [As/mol] represents the Faraday constant. Moreover, it is taken into account the absolute supply pressure of fuel P_{fuel} [atm] and air P_{air} [atm], the flow rate of fuel V_{fuel} [l/min] and air V_{air} [l/min] as well as the percentage of hydrogen in the fuel x [%] and of oxygen in the air y [%].

$$U_{H2} = \frac{60000 R T_{fc} I_{fc}}{z F P_{fuel} V_{fuel} x} \tag{34}$$

$$U_{O2} = \frac{60000 R T I_{fc}}{z F P_{air} V_{air} y} \tag{35}$$

Hence, the partial pressures P_{H2} (Eq. (36)), P_{H2O} (Eq. (37)) and P_{O2} (Eq. (38)) and the Nernst voltage E_n (Eq. (39)) can be derived from the aforementioned rates of conversion, where w [%] corresponds to the percentage of water vapor.

$$P_{H2} = (1 - U_{H2}) x P_{fuel} \tag{36}$$

$$P_{H2O} = (w + 2 y U_{O2}) P_{air} \tag{37}$$

$$P_{O2} = (1 - U_{O2}) y P_{air} \tag{38}$$

$$E_n = \begin{cases} 1.229 + (T - 298) \frac{-44.43}{zF} + \frac{RT}{zF} \ln \left(P_{H2O} \sqrt{P_{O2}} \right), \\ \text{if } T_{fc} \leq 373.15 \text{ K} \\ \\ 1.229 + (T - 298) \frac{-44.43}{zF} + \frac{RT}{zF} \ln \left(\frac{P_{H2O} \sqrt{P_{O2}}}{P_{H2O}} \right), \\ \text{if } T_{fc} > 373.15 \text{ K} \end{cases} \tag{39}$$

The specification parameters (Table 3) were estimated from typical values found on Ballard Power manufacturer datasheets [79].

Moreover, the PEM fuel cell stack degradation is calculated according to the model proposed by Chen et al. [80]. In this case, the system lifetime is quantified based on the voltage drop rate of the cells V_{drop} [µV/h] along the operation. This variable is given by Eq. (40), where n_1, t_1, n_2, t_2 stand for the number of start-stop cycles per hour, the idling power condition time per hour, power transition times per hour and high power condition time per hour, respectively. The

Table 3
PEM fuel cell stack parameters.

Rated current	200 A
Rated voltage	202 V
Maximum power	90 kW
Number of cells	309
Operating temperature	338 K
Storage tank pressure	70 MPa

voltage degradation rates for the constants λ_{ss}, λ_{idl}, λ_{chg} and λ_{hgh} are 13.79 µV/cycle, 8.66 µV/h, 0.418 µV/cycle, 10 µV/h, and 42.16 µV/h, respectively.

$$V_{drop} = n_1 \lambda_{ss} + t_1 \lambda_{idl} + n_2 \lambda_{chg} + t_2 \lambda_{hgh} \tag{40}$$

Hence, the fuel cell lifetime L_{fc} [h] is determined by Eq. (41), in which ΔV [V] corresponds to the allowable voltage loss for each cell until the system reaches its end of life. According to the literature [81,82], a criterion that indicates the end of life of a fuel cell system can be estimated by 10% voltage loss. The variable k_{fc}, on the other hand, is a constant that equals to approximately 1.72 [83].

$$L_{fc} = \frac{\Delta V}{k_{fc} V_{drop}} \tag{41}$$

3. Fuzzy logic control

In the literature, the fuzzy logic approach has been widely employed in different areas of engineering such as renewable energy systems [84–86], thermal systems [87,88], biomedical systems [89], and energy storage systems [90–92]. Moreover, this control method has successfully been used for energy management control of plug-in hybrid electric [67,93,94], hybrid electric [95,96], fully electric [61,97], and fuel cell electric vehicles [58], as well as vehicle handling [98–100] and gear shifting control [101,102]. Thus, the fuzzy logic controllers, which feature anti-disturbance and robustness, are adopted in this study for the power distribution control between front and rear drive systems, fuel cell stack and HESS, and battery and ultracapacitor.

It is also worth pointing out that this work tunes the fuzzy controllers' design parameters by means of an optimization procedure. This is due to the fact that the formulation of the membership functions, rules and weights are usually determined according to experience acquired from experts, which makes the optimization of fuzzy controllers a convoluted task to accomplish. In this sense, the use of i-AWGA method for the formulation of the fuzzy control parameters ensures an unbiased formulation and optimal results.

The Mamdani inference method was applied for the controllers, as it has achieved promising results in previous studies [61,102,103]. In the current work, the implementation of this method was based on the Matlab™ fuzzy logic toolbox.

3.1. Power split control between front and rear drive systems

The power demand is initially distributed between the front and rear drive systems according to the first fuzzy logic controller. In this case, the fuzzy control consists of three different inputs (rear system efficiency η_R, front system efficiency η_F, and required torque T_{req}) and one output P_S. The latter varies from 0 to 1 and determines the amount of power delivered to each drive system (see Eqs. (3) and (4)). In addition, the membership functions are composed of three levels (low, medium, and high), as depicted by Fig. 5a. In this work, linear membership functions were chosen, as they have a simpler formulation, cause less computational burden, and are vastly used in engineering applications [104]. The use of trapezoidal functions was due to the fact that the trapezoidal shapes provide a wider range of feasible configurations as compared to triangular ones.

In this sense, the vector $\mathbf{MF_{PS}}$ (Eq. (42)) denotes the membership functions parameters that are tuned by the optimization procedure, in which T_{ri}, E_{Fi}, E_{Ri}, and P_{Si} represent the function variables for required torque, front system efficiency, rear system efficiency, and power split fraction, respectively. The fuzzy controller's rules R_{Pi} and weights W_{Pi}, on the other hand, are combined into the vector $\mathbf{RW_{PS}}$, as expressed by Eq. (43). Table 4 shows the optimizable fuzzy output rules for all the possible combinations of the inputs' levels L_d (low), M_d (medium) and H_d (high). Regarding the defuzzification method D_{z1}, it was defined as centroid in order to avoid abrupt changes in

(a) Front and rear traction systems power split

(b) Fuel cell - HESS power split

(c) Battery-ultracapacitor HESS power split
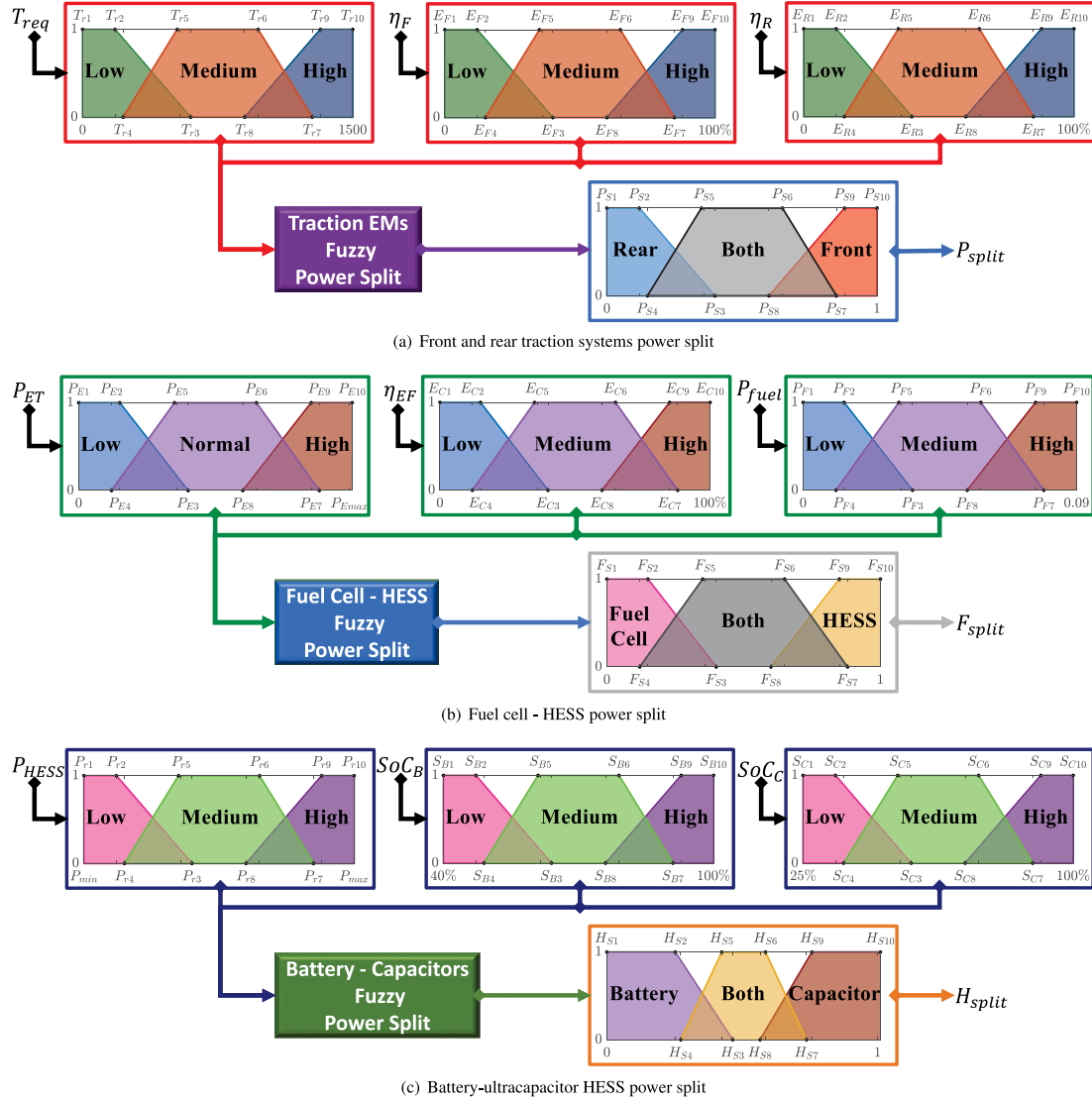
Fig. 5. Fuzzy controllers.

Table 4
Fuzzy control rules.

Input 1	Input 2	Input 3		
		L_d	M_d	H_d
L_d	L_d	R_1 W_1	R_2 W_2	R_3 W_3
	M_d	R_4 W_4	R_5 W_5	R_6 W_6
	H_d	R_7 W_7	R_8 W_8	R_9 W_9
M_d	L_d	R_{10} W_{10}	R_{11} W_{11}	R_{12} W_{12}
	M_d	R_{13} W_{13}	R_{14} W_{14}	R_{15} W_{15}
	H_d	R_{16} W_{16}	R_{17} W_{17}	R_{18} W_{18}
H_d	L_d	R_{19} W_{19}	R_{20} W_{20}	R_{21} W_{21}
	M_d	R_{22} W_{22}	R_{23} W_{23}	R_{24} W_{24}
	H_d	R_{25} W_{25}	R_{26} W_{26}	R_{27} W_{27}

the power split percentage, which would be difficult to achieve in real-world driving scenarios [105].

$$\left[\mathbf{MF_{PS}}\right]_{1\times32} = \left[T_{r2}\ T_{r3}\ldots T_{r8}\ T_{r9}\ E_{F2}\ E_{F3}\ldots\right.$$
$$\left. E_{F8}\ E_{F9}\ E_{R2}\ E_{R3}\ldots E_{R8}\ E_{R9}\ P_{S2}\ P_{S3}\ldots P_{S8}\ P_{S9}\right] \quad (42)$$

$$\left[\mathbf{RW_{PS}}\right]_{1\times54} = \left[R_{p1}\ R_{p2}\ \ldots\ R_{p27}\ W_{p1}\ W_{p2}\ldots W_{p27}\right] \quad (43)$$

Furthermore, it is important to mention that, to achieve a feasible fuzzy logic, the control parameters must satisfy the constraints C_{fz}, given by Eq. (44), where I/O_i stands for the input or output membership functions' points, R_{jk} denotes the output rules and W_{jk} represent the fuzzy weights.

$$C_{fz} = \begin{cases} I/O_1 < I/O_2 < I/O_3 \\ I/O_4 < I/O_5 < I/O_6 < I/O_7 \\ I/O_8 < I/O_9 < I/O_{10} \\ I/O_1 < I/O_3 < I/O_8 < I/O_{10} \\ I/O_1 < I/O_4 < I/O_3 \\ I/O_8 < I/O_7 < I/O_{10} \\ I/O_2 < I/O_5 < I/O_6 < I/O_9 \\ 1 \le R_{jk} \le 3 \\ 0 \le W_{jk} \le 1 \end{cases} \quad (44)$$

3.2. Power split control between fuel cell and HESS

A fuzzy-logic controller to determine the power distribution between the PEM-based fuel cell and HESS is also needed to achieve greater energy efficiency and the amount of power that should be supplied by each energy source. Thus, the fuzzy inputs and output are depicted in Fig. 5b, where P_{ET} [W], η_{EF} and P_{fuel} [l/s] represent the power demand, the fuel cell system efficiency and the hydrogen fuel rate, respectively. The vector $\mathbf{MF_{FH}}$, expressed by Eq. (45), comprises the trapezoidal input/output membership function parameters, while $\mathbf{RW_{FH}}$ (Eq. (46)) represents the rules R_{hi}, weights W_{hi} and defuzzification method D_{z2} of the fuzzy controller. The value of D_{z2} can be 1 (centroid), 2 (bisector), 3 (middle of maximum), 4 (largest of maximum) or 5 (smallest of maximum). Furthermore, the fuzzy rules in Table 4 and the constraints in Eq. (44) also apply to this control system.

$$[\mathbf{MF_{FH}}]_{1\times32} = [P_{E2}\ P_{E3}\ ...\ P_{E8}\ P_{E9}\ E_{C2}\ E_{C3}\ ... \\ E_{C8}\ E_{C9}\ P_{F2}\ P_{F3}\ ...\ P_{F8}\ P_{F9}\ F_{S2}\ F_{S3}\ ...\ F_{S8}\ F_{S9}] \quad (45)$$

$$[\mathbf{RW_{FH}}]_{1\times55} = [R_{f1}\ R_{f2}\ ...\ R_{f27}\ W_{f1}\ W_{f2}\ ...W_{f27}\ D_{z2}] \quad (46)$$

Lastly, P_S represents the output value for this fuzzy controller, in which the variable has unitary range and defines the fraction of the requested power provided by fuel cell and battery-ultracapacitor HESS. Such power split can be expressed by Eqs. (47) and (48), where P_{req} [W], P_{fc} [W] and P_{HESS} [W] correspond to the required power, the requested power for the fuel cell and requested power for the HESS, respectively

$$P_{fc} = P_{req}P_S \quad (47)$$

$$P_{HESS} = P_{req}(1 - P_S) \quad (48)$$

3.3. HESS power split control

Analogously to the aforementioned power split controllers, the battery-ultracapacitor HESS energy management is carried out by a fuzzy-logic controller, composed of three inputs and one output, as depicted by Fig. 5c. The fuzzy inputs are characterized by the actual power P_{HESS} [W] supplied by the HESS, the battery state of charge SoC_B and the ultracapacitor state of charge SoC_C. Hence, the vectors $\mathbf{MF_{HS}}$ (Eq. (49)) and $\mathbf{RW_{HS}}$ (Eq. (50)) correspond to the input/output membership functions' parameters, and the fuzzy rules R_{hi}, weights W_{hi} and defuzzification method D_{z3}, respectively. The variables $[P_{ri}\ S_{Bi}\ S_{Ci}]$ represent the fuzzy inputs, while H_{Si} stands for the output, which presents a unitary-range value, as the other fuzzy controllers.

$$[\mathbf{MF_{HS}}]_{1\times32} = [P_{r2}\ P_{r3}\ ...\ P_{r8}\ P_{r9}\ S_{B2}\ S_{B3}\ ...\ S_{B8}\ S_{B9}\ ... \\ S_{C2}\ S_{C3}\ ...\ S_{C8}\ S_{C9}\ H_{S2}\ H_{S3}\ ...\ H_{S8}\ H_{S9}] \quad (49)$$

$$[\mathbf{RW_{HS}}]_{1\times55} = [R_{h1}\ R_{h2}\ ...\ R_{h27}\ W_{h1}\ W_{h2}\ ...W_{h26}\ W_{h27}\ D_{z3}] \quad (50)$$

The output variable H_S defines the power split fraction performed by the battery and ultracapacitor pack. Thus, the requested power for the former P_{batt} [W] and the latter P_{cap} [W] are expressed by Eq. (51) and Eq. (52), respectively. In this case, the ultracapacitor is actuated in discharge mode according to the parameter S_{reg} (Eq. (53)), which prevents such system to overdischarge, that is, any circumstance in which the ultracapacitor state of charge SoC_C has reached a value lower than 25%. Additionally, this state variable S_{reg}, once the ultracapacitor has previously reached a SoC_C of 25%, avoids the discharge of the system while it has not regenerated sufficient energy to achieve the minimum state of charge SoC_{reg} that can vary from 35% to 95% based on the optimization procedure described in Section 4.

$$P_{batt} = \begin{cases} P_{HESS}H_S, & \text{if } S_{reg} = 0 \text{ and } P_{HESS} > 0 \\ P_{HESS}, & \text{if } S_{reg} = 1 \text{ and } P_{HESS} > 0 \\ 0, & \text{if } P_{HESS} \leq 0 \end{cases} \quad (51)$$

$$P_{cap} = \begin{cases} P_{HESS}(1 - H_{S(F/R)}), & \text{if } S_{reg} = 0 \text{ and } P_{HESS} > 0 \\ 0, & \text{if } S_{reg} = 1 \text{ and } P_{HESS} > 0 \\ P_{HESS}, & \text{if } P_{HESS} \leq 0 \end{cases} \quad (52)$$

$$S_{reg}(t) = \begin{cases} 1, & \text{if } \begin{cases} SoC_C(t) < 25\%, \text{ or:} \\ S_{reg}(t - \varDelta t) = 1 \text{ and } SoC_C(t) < SoC_{reg} \end{cases} \\ 0, & \text{if } \begin{cases} SoC_C(t) \geq SoC_{reg}, \text{ or:} \\ S_{reg}(t - \varDelta t) = 0 \text{ and } SoC_C(t) \geq 25\% \end{cases} \end{cases} \quad (53)$$

4. Optimization procedure

The formulation of the multi-objective optimization problem is discussed in this section, along with each of the optimization criteria that were taken into consideration in this work. In addition, the optimal powertrain design variables and fuzzy logic controller parameters are achieved using the evolutionary algorithm procedure that are both described and implemented.

4.1. Optimization criteria and design parameters

An evolutionary algorithm method serves in this study as the foundation for the formulation of the optimization problem. In this way, a chromosome vector $\mathbf{X}$ stores as genes the fuzzy logic-based energy management control and FCHEV powertrain design parameters, as expressed by Eq. (54).

$$[\mathbf{X}]_{1\times271} = [Q_{nom}\ V_{nom}\ T_{maxF}\ \omega_{TcF}\ T_{maxR}\ \omega_{TcR}\ Cap\ N_s\ N_p\ ... \\ SoC_{reg}N_d\ \mathbf{MF_{PS}}\ \mathbf{RW_{PS}}\ \mathbf{MF_{FH}}\ \mathbf{RW_{FH}}\ \mathbf{MF_{HS}}\ \mathbf{RW_{HS}}] \quad (54)$$

In the first optimization criterion f_1, it is considered the FCHEV driving range D_R [km], so that the autonomy of the vehicle can be maximized, as expressed by Eq. (55). In this study, the range is quantified until the battery reaches its minimum allowable SoC value of 40%. At the same time, the maximum hydrogen cost was considered 4 kg, which is close to typical tank capacities that current FCHEVs available in the market can hold. It is important to highlight that, in this work, the driving range is defined by when the battery reaches its minimum state of charge ($SoC = 40\%$). Hence, the configurations can either consume all the available hydrogen stored in the tanks (4 kg) through the high use of the fuel cell or opt to use the battery-ultracapacitor HESS as the main power source, consuming only part of the stored fuel and actuating the fuel cell only under specific driving profiles. This decision will be made by the power management control strategy that may target the minimization of fuel used, the maximization of driving range or the balance between these two factors.

$$f_1(\mathbf{X}) = \max\left(D_R(\mathbf{X})\right) \quad (55)$$

Additionally, the minimization of the hybrid energy storage system size is the second criterion f_2 (Eq. (56)), which directly influences the vehicle's overall mass and the aforementioned driving autonomy.

$$f_2(\mathbf{X}) = \min\left(M_{HESS}(\mathbf{X})\right) \quad (56)$$

The third criterion f_3 (Eq. (57)) is to minimize the hydrogen consumption H_{cons} [kg/100 km] of the FCHEV configuration under the combined driving profile considered in this work (see Fig. 2). Since the cost of hydrogen fuel remains a significant obstacle for the fuel cell electric vehicle market, this factor receives high priority in the optimization process and is directly related to the operating cost of completing the desired path.

$$f_3(\mathbf{X}) = \min\left(H_{cons}(\mathbf{X})\right) \quad (57)$$

Finally, the last optimization criterion f_4 is associated to the minimization of the power source degradation. The factor L_{PS} (Eq. (58)) is defined by an adaptive weight calculation that takes into consideration the battery state of health SoH and the voltage drop rate V_{drop} of the

PEM fuel cell along the cycles. Hence, the criterion f_4 is given by Eq. (59).

$$L_{PS}(\mathbf{X}) = \frac{SoH^{max} - SoH(\mathbf{X})}{SoH^{max} - SoH^{min}} + \frac{V_{drop}(\mathbf{X}) - V_{drop}^{min}}{V_{drop}^{max} - V_{drop}^{min}} \quad (58)$$

$$f_4(\mathbf{X}) = \min\left(L_{PS}(\mathbf{X})\right) \quad (59)$$

4.2. Interactive adaptive-weight genetic algorithm (i-AWGA)

In this study, the optimization problem is solved by the i-AWGA method proposed by Gen et al. [106]. This genetic algorithm method was used, since it has been used successfully in previous works to optimize multiple complex systems with different goals such as fully electric vehicle powertrain design [61,97], plug-in hybrid electric vehicle powertrain design [67,105], hydraulic hybrid vehicle powertrain design [19,107], multi-speed transmission design [108,109] and shift schedule control [102,110]. This is due to the fact that this optimization method presents a wide search for the most compromised solutions, being not limited to local optimum. Furthermore, the procedure has been previously compared to results obtained by the particle swarm optimization method [98], which showed that both methods achieved similar outcomes.

The i-AWGA fitness function F_t (Eq. (60)), which takes into consideration the maximum and minimum outcomes for each optimization criterion, is used to classify the members of the population. The minimum and maximum values for each optimization criterion are selected among all existing solutions presented in the current generation of the population. With the population evolution, the new solutions tend to be better than the previous ones, while the worst results are eliminated from the population according to the population size rules. Therefore, these minimum and maximum values applied change at each generation. The calculation also includes a penalty factor P_p, which assumes a value of one for the first ranked members and zero for the members from the second ranking onwards.

$$F_t(\mathbf{X}) = \frac{f_1(\mathbf{X}) - f_1^{min}}{f_1^{max} - f_1^{min}} + \frac{f_2^{max} - f_2(\mathbf{X})}{f_2^{max} - f_2^{min}} + \frac{f_3^{max} - f_3(\mathbf{X})}{f_3^{max} - f_3^{min}} + \frac{f_4^{max} - f_4(\mathbf{X})}{f_4^{max} - f_4^{min}} + P_p(\mathbf{X}) \quad (60)$$

Hence, this method weighs the importance of each optimization criterion and makes it more likely that the best candidates will crossover or mutate, which makes the evolution process shorter. The candidate with the greatest fitness (that is, most compromised with the optimization criteria) will also have the highest probability of selection S_P, which is determined as a function of the population size P_{size}, as expressed by Eq. (61).

$$S_P(\mathbf{X}) = \frac{F_t(\mathbf{X})}{\sum_{X=1}^{P_{size}} Ft(\mathbf{X})} \quad (61)$$

Twenty chromosomal pairs ($\mathbf{X}_1$ and $\mathbf{X}_2$) are chosen each generation to be randomly merged via the crossover process, creating a new chromosome called $\mathbf{X}_{cr}$. Once the optimization criteria are met by this configuration, the merged member $\mathbf{X}_{cr}$ is simulated and added to the current population. Additionally, the chance of choosing the design variables from $\mathbf{X}_1$ and $\mathbf{X}_2$ is equal.

Additionally, a mutation operator is implemented in order to ensure population variety. The chromosomes $\mathbf{X}_1$, $\mathbf{X}_2$, and $\mathbf{X}_{cr}$'s design variables are randomly modified (with a chance of 50%), resulting in the new members $\mathbf{X}_{M1}$, $\mathbf{X}_{M2}$, and $\mathbf{X}_{Mcr}$, respectively. Then, if the required minimum performance criteria were met, those chromosomes were introduced into the population after being assessed using the optimization constraints $C(\mathbf{X})$ described in Eq. (62). In these constraints, a minimum speed correlation coefficient $COR_{min}(\mathbf{X})$ is considered, so that the FCHEV configurations with poor acceleration performance can be avoided. This variable is defined by Eq. (63), as a function of the target speed from the driving profile V_c and the actual vehicle speed V.

$$C(\mathbf{X}) = \begin{cases} 20 \text{ Ah} \leq Q_{nom} \leq 70 \text{ Ah} \\ 100 \text{ V} \leq V_{nom} \leq 300 \text{ V} \\ 1 \leq N_s \leq 25 \\ 1 \leq N_p \leq 5 \\ 50 \text{ Nm} \leq T_{max} \leq 300 \text{ Nm} \\ 26 \text{ rad/s} \leq \omega_{Tc} \leq 314 \text{ rad/s} \\ 3.5 \leq N_d \leq 7 \\ 35\% \leq SoC_{reg} \leq 95\% \\ COR_{min}(\mathbf{X}) \geq 0.99 \\ D_R \geq 94 \text{ km} \end{cases} \quad (62)$$

$$COR = \sqrt{\frac{\left(\sum \left(V_c - \bar{V}_c\right)\left(V - \bar{V}\right)\right)^2}{\sum \left(V_c - \bar{V}_c\right)^2 \sum \left(V - \bar{V}\right)^2}} \quad (63)$$

Finally, the population size is constrained by a maximum member count P_{limit} of 200. Once the population reaches this threshold, the highest Pareto ranked solutions are eliminated. The population size is reset by the requirement that $P_{limit} = P_{limit} + 100$, preventing the removal of the whole population in the event that the Pareto frontier (i.e., the first ranking solutions) exhibits a larger size than P_{limit} [111]. In case that the Pareto frontier has been stationary for more than 10 generations, it can be concluded that the evolutionary process reached its convergence.

The flowchart depicted in Fig. 6 shows each step of the optimization procedure that was employed in this study. As previously presented by Eq. (54), the evolutionary algorithm deals with 271 design parameters, that characterize electric drive system, HESS (battery and ultracapacitor), and power management controllers.

5. Optimization results and discussion

Once the convergence is achieved, the Pareto frontier of non-dominated solutions obtained by the optimization procedure defines the optimum FCHEV configurations, as depicted by Fig. 7. The solutions that offer the minimum (or maximum) values of each objective function are highlighted in such Pareto frontier. Those configurations represent the maximum driving range (max f_1), the minimum HESS mass (min f_2), the minimum hydrogen consumption (min f_3), and the minimum power sources degradation factor (min f_4). In addition, the most compromised configuration in terms of the trade-off (max F_t) between the four taken into account criteria is likewise examined. The optimization results and design parameters of the powertrain for each one of the optimal configurations is presented in Table 5.

It is possible to observe from the Pareto frontier that a reduction in the hydrogen consumption leads to the decrease of the driving autonomy, as shown in Fig. 7b. However, this changing pattern is clearly modified when solutions such as max f_1, min f_2, min f_4 and max F_t consume all the hydrogen fuel stored in the tank (4 kg) during the driving cycle. This is due to the fact that those solutions present the same amount of H_2 fuel used [kg] and, for those configurations, the greater the driving range, the lower the hydrogen consumption H_{cons} [kg/100 km].

Regarding the HESS size, Fig. 7a illustrates that a heavy HESS does not necessarily represent the increase of the autonomy. In fact, FCHEV powertrain architectures, which already carry large hydrogen tanks, require moderate size of the auxiliary power unit, as significant weight may eventually reduce their driving range. At the same time, the HESS size can influence the hydrogen consumption of the vehicle (Fig. 7f), since larger HESS can effectively meet higher power demands, alleviating the fuel cell stack operation and, consequently, maximizing the fuel efficiency.
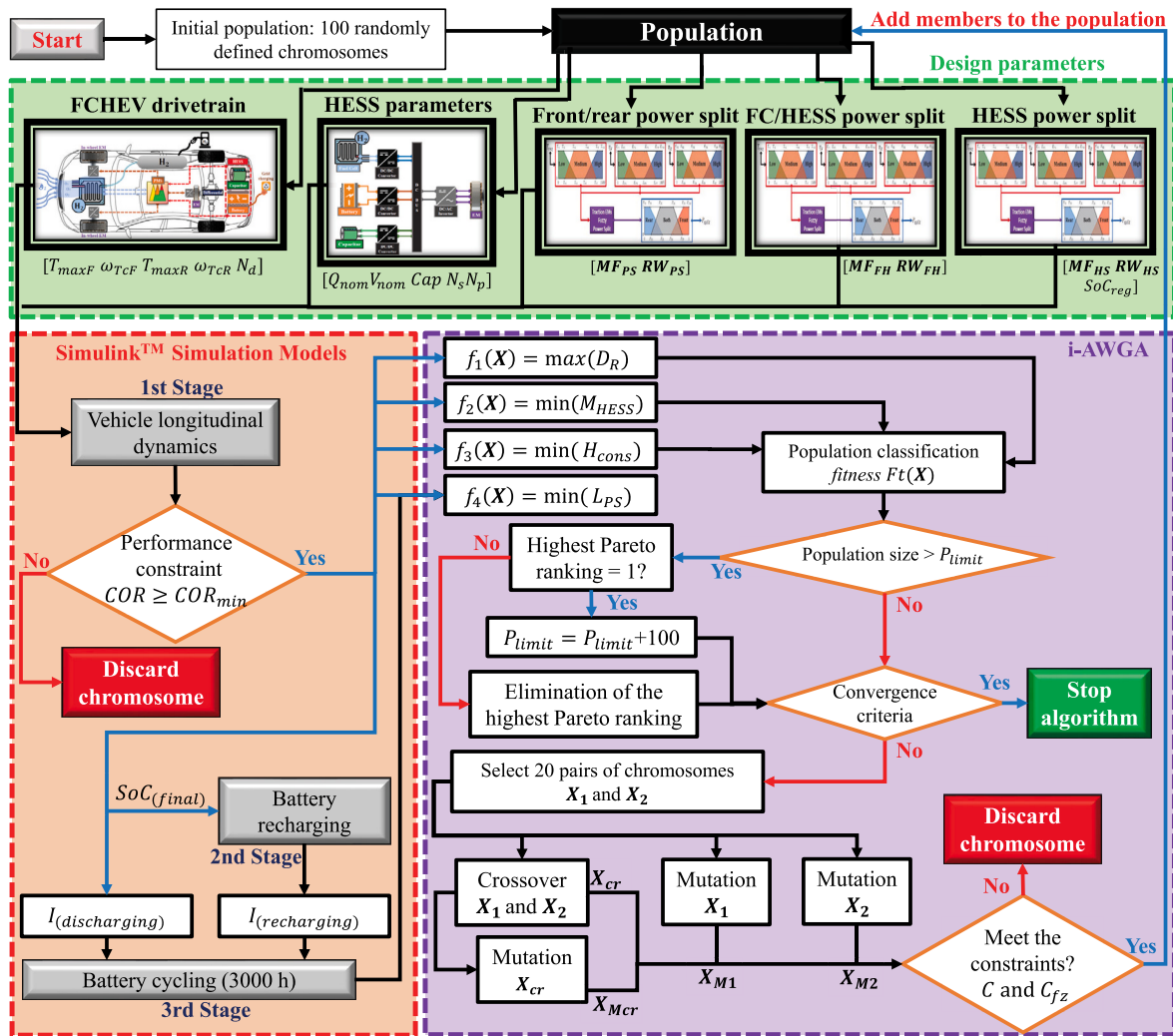
Fig. 6. Optimization flowchart.

Table 5
Optimization results.

Results	Optimal FCHEV configurations				
	Max. autonomy $\max(f_1)$	Min. HESS mass $\min(f_2)$	Min. H_2 used $\min(f_3)$	Min. degradation $\min(f_4)$	Best trade-off $\max(Ft)$
H_2 consumption [kg/100 km]	0.8659	0.9991	0.5521	0.9474	0.9009
Driving range [km]	461.96	400.41	95.15	422.23	444.08
Performance $COR(X)$	0.9978	0.9916	0.9907	0.9910	0.9914
Battery mass M_{bat} [kg]	64.38	25.71	63.37	53.65	45.05
UC mass M_{cap} [kg]	37.50	21	37.50	45	24
Battery SoH	0.9960	0.9975	0.9860	0.9989	0.9979
Battery life [h]	9305	9024	8062	9343	9276
FC voltage drop V_{drop} [μV/h]	4.946	4.371	9.848	4.451	4.140
FC lifespan L_{fc} [h]	7688	8699	3861	8541	9184
Recharging time C_t [h]	2.59	2.62	2.42	2.39	2.58
$\frac{\text{Driving Range}}{\text{Energy storage mass}}$ [km/kg]	1.91	2.14	0.40	1.77	2.12
Chromosomes					
Q_{nom} [Ah]	38.87	26.21	44.34	40	30.15
V_{nom} [V]	248.43	147.14	214.37	201.17	224.11
T_{maxF} [Nm]	221.56	162.93	159.46	167.13	177.85
ω_{TcF} [rpm]	378.36	342.15	397.37	356.42	342.15
T_{maxR} [Nm]	27.99	50.13	27.14	30.77	27.99
ω_{TcR} [rpm]	777.51	761.14	650.79	761.14	650.79
Cap	10	1	10	11	1
N_s	3	7	3	3	8
N_p	1	1	1	1	1
N_d	6.11	6.16	6.68	5.27	6.16
SoC_{reg} [%]	55.92	74.86	56.57	46.08	55.45

(a) $f_1 \times f_2$

(b) $f_1 \times f_3$

(c) $f_4 \times f_1$

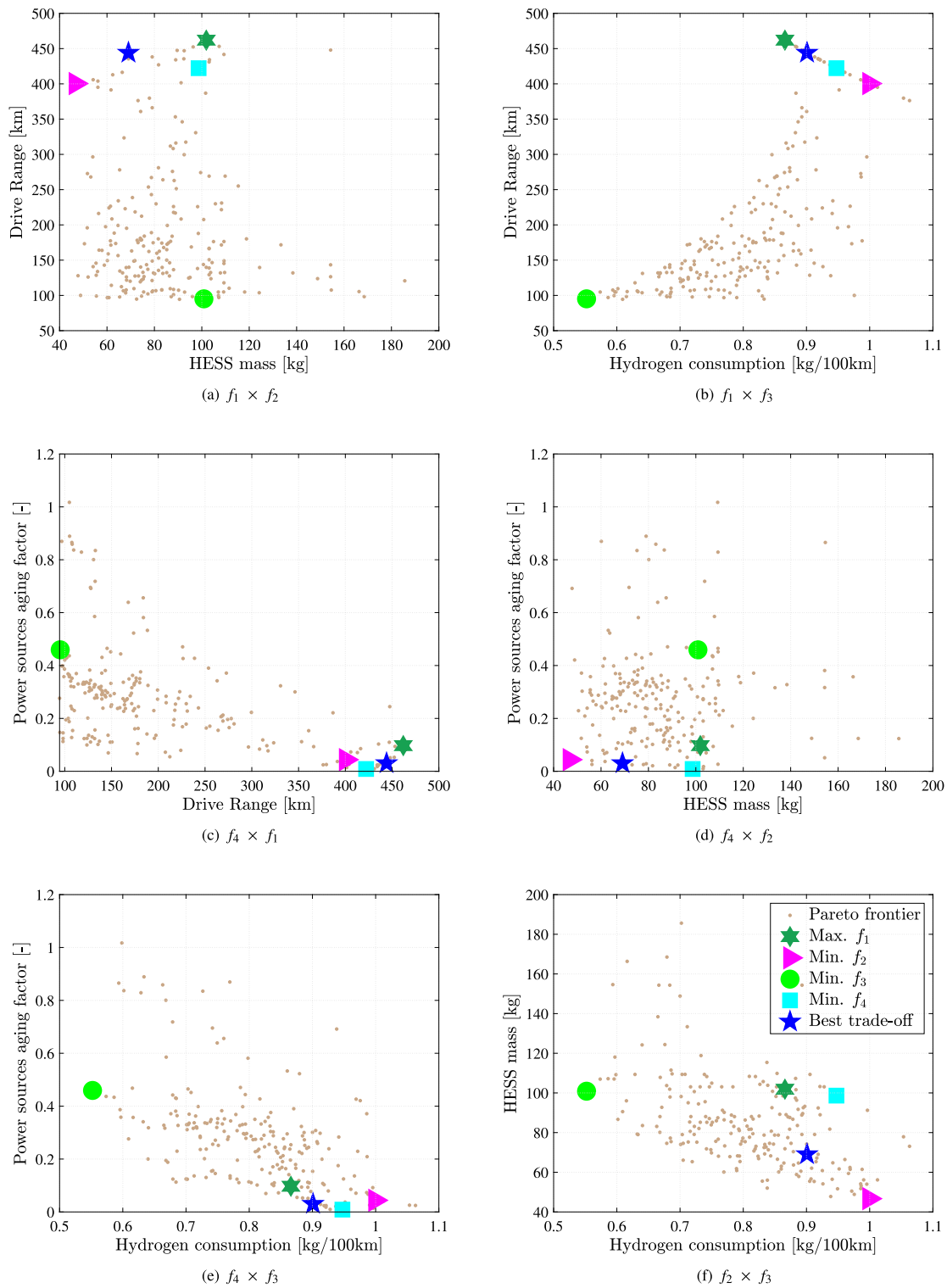(d) $f_4 \times f_2$

(e) $f_4 \times f_3$

(f) $f_2 \times f_3$

Fig. 7. Optimized solutions.

Furthermore, Fig. 7c shows that the reduction of the degradation of the power sources (fuel cell and battery) is followed by the increase of driving range. The hydrogen consumption, on the other hand, is increased to maintain a longer system lifespan, as shown by Fig. 7e. This can be explained by the fact that configurations that aim the minimization of the hydrogen fuel cost used more the HESS in high power demand profiles, thereby significantly reducing the battery lifetime. Since the driving range is limited to the minimum value of the battery *SoC* (40%), those solutions prioritize the HESS operation to

save hydrogen fuel. In this sense, aging-aware power management control strategies are of great importance to simultaneously achieve high autonomy, hydrogen fuel efficiency, and fuel cell and battery longevity. Fig. 8 depicts a comparison between the optimal configurations with regard to energy efficiency, system size, charging time, and power source degradation.

As can be seen in Table 5, max f_1 solution reached a driving autonomy of approximately 462 km, in which the vehicle is equipped with a 102 kg HESS. Despite the large auxiliary energy storage system to
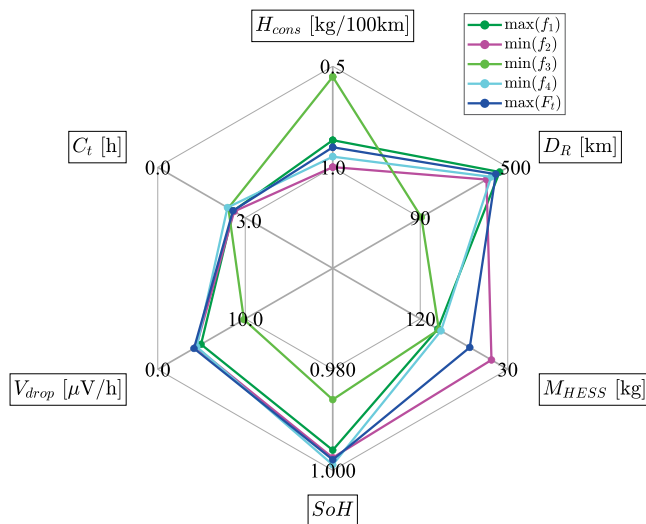
Fig. 8. Spider plot: optimal FCHEV configurations.

maximize the driving range, this configuration, which has the sixth-highest fitness F_t value in the Pareto frontier, presented hydrogen consumption of 0.8659 kg/100 km, which represents a reduction of 15.4%, 9.41%, and 3.88% when compared to the min f_2, min f_4 and max F_t solutions, respectively. At the same time, the increase of fuel efficiency obtained by max f_1 solution is followed by the shorter fuel cell lifespan (L_{fc}). In comparison to min f_4 and max F_t configurations, max f_1 showed a reduction of 13.15%, 11.09%, and 19.46% in L_{fc}.

The min f_2 solution, on the other hand, presents a compact HESS of 46.71 kg. Although the small HESS led to the reduction of the driving autonomy (decrease of 15.37%, 5.17%, and 10.91% compared against max f_1, min f_4, and max F_t, respectively), the ratio between range and energy storage mass was the highest among the optimal configurations, as described in Table 5, and the fitness value is the fourth highest in the Pareto frontier.

Regarding min f_3, the hydrogen fuel consumption was substantially decreased, which can be explained by the short driving autonomy (95.15 km). Additionally, this FCHEV configuration is equipped with a HESS of significant size (100.9 kg) that can be an effective alternative to increase fuel efficiency. Fig. 8 illustrates the results of this configuration when compared to the other optimal configurations. Although the solution consumes less hydrogen per each 100 km driven, the energy management strategy does not favor the fuel cell lifetime, presenting higher number of start-stop cycles per hour and significant idling time (almost 30% of the driving cycle). Since this solution does not present a reasonable balance between all the optimization criteria considered in this study, it only has the 132nd best fitness among the 219 non-dominated configurations.

The simulation results for the optimized solution min f_4 with minimized power source degradation factor L_{PS} is likewise presented in Table 5. In this case, the configuration prioritizes the fuel cell and battery cycle life, presenting a HESS size (97.65 kg) higher than the average of the optimized solutions. The choice for a robust HESS avoids overloading of the main and secondary power sources and, consequently, the shortening of their lifespans. For such HESS, the configuration features a larger ultracapacitor pack (45 kg), so that it can be used as a power buffer unit in high demand driving conditions. Another important drawback of this solution is that the ratio between driving autonomy and energy storage mass is 7.91%, 20.91% and 19.77% lower than those of max f_1, min f_2 and max F_t, respectively. In this sense, min f_4 is ranked as the 23rd in the Pareto frontier.

Finally, the best trade-off solution max F_t features a 69.05 kg HESS, while keeping an extended driving range and long energy source lifespan. As depicted in Fig. 8, this configuration managed to balance the

optimization criteria, achieving the optimality for the FCHEV power-train architecture proposed in this study. In addition, other important factors such as correlation performance coefficient COR, recharging time C_t and autonomy-to-mass ratio were not compromised in this case.

Fig. 9 depicts the simulation results for the best trade-off FCHEV configuration, in which it is possible to observe the hydrogen consumption, battery state of charge SoC_B and ultracapacitor state of charge SoC_C profiles along the repeated driving cycles. In this case, the power management control strategy consists of a distributed use of the battery pack and fuel cell stack, demanding deep discharges in the ultracapacitor pack for the high power routes. Such strategy allows the extension of the power sources (fuel cell and battery) lifetime, while ensuring high driving range. As illustrated by Fig. 9, once the vehicle runs out of hydrogen, the battery replaces the fuel cell stack as the main power source. As it could be expected, at this moment, the battery starts to meet a higher power demand, thereby increasing the discharging rate. As previously mentioned, the driving range is defined by when the battery SoC_B achieves its minimum allowable value of 40%.

Finally, Fig. 10 shows the fuzzy controller surface's optimal configurations for the best trade-off solution.

5.1. Cost–benefit analysis

This section compares the selected FCHEV solutions of the current study with different optimal electrified vehicle powertrain configurations obtained in earlier published works through the evaluation of their ownership and operating costs. This comparative analysis considers a single HESS-equipped EV [97], a dual HESS-equipped EV [97], a EV equipped only with a battery as the energy storage system [98], and an electric-hydraulic hybrid vehicle (EHHV) [107].

Table 6 presents the cost results for each type of propulsion architecture. The single HESS-based and dual HESS-based EV configurations were optimized with focus on the maximization of the driving range, front and rear battery state of health, and minimization of the battery-ultracapacitor HESS size. The optimization of the single battery-based EV, on the other hand, aimed to minimize the electric propulsion system size, the driver action, improving the vehicle handling, quantified by means of the root-mean-square deviation of the steering angle δ_{rms}, as well as maximize the final battery state of charge. Lastly, the optimization criteria considered in the design and control of the EHHV powertrain were the autonomy, battery and hydraulic system weight, and battery state of health. Notice that those studies consider three criteria for the optimization, while the current work takes into account four different objective functions.

In the analysis, the cost of the powertrain components were estimated, so that the cost of ownership and cost-to-range ratio could be determined for each vehicle configuration. For instance, the lithium-ion battery cost was defined according to the ratio of US\$ 165/kWh, as reported by [114,115]. Regarding the electric motors, their costs were calculated based on a database from the market described in [67]. The cost of the fuel cell stack was likewise estimated by technical reports available in the literature [116]. Finally, the price of the ultracapacitor pack was given by the ratio of US\$ 66640 per 1 kWh of stored energy, as reported by [117].

As described in Table 6, the best trade-off FCHEV configuration achieved an overall cost-to-autonomy ratio of 31.28, which stands for a reduction of 26.57%, 23.11%, 63.59%, 63.26% when compared against the optimal dual HESS-based EV, single HESS-based, single battery-based EV, and EHHV, respectively. Hence, it is possible to assume that the max (F_t) FCHEV solution presented the highest benefit–cost ratio among the investigated configurations. The max (f_1) and min (f_2) also presented promising results, with decrease of up to 69.62% with respect to other electrified vehicle powertrain topologies.

However, it is noteworthy to mention that the min (f_3) solution showed an important disadvantage among the analyzed configurations, as it featured a substantially higher cost-to-range ratio. This can be
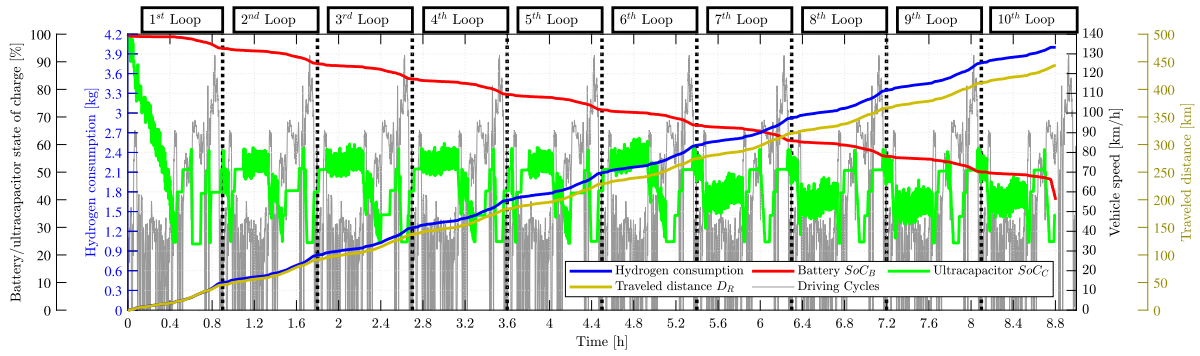
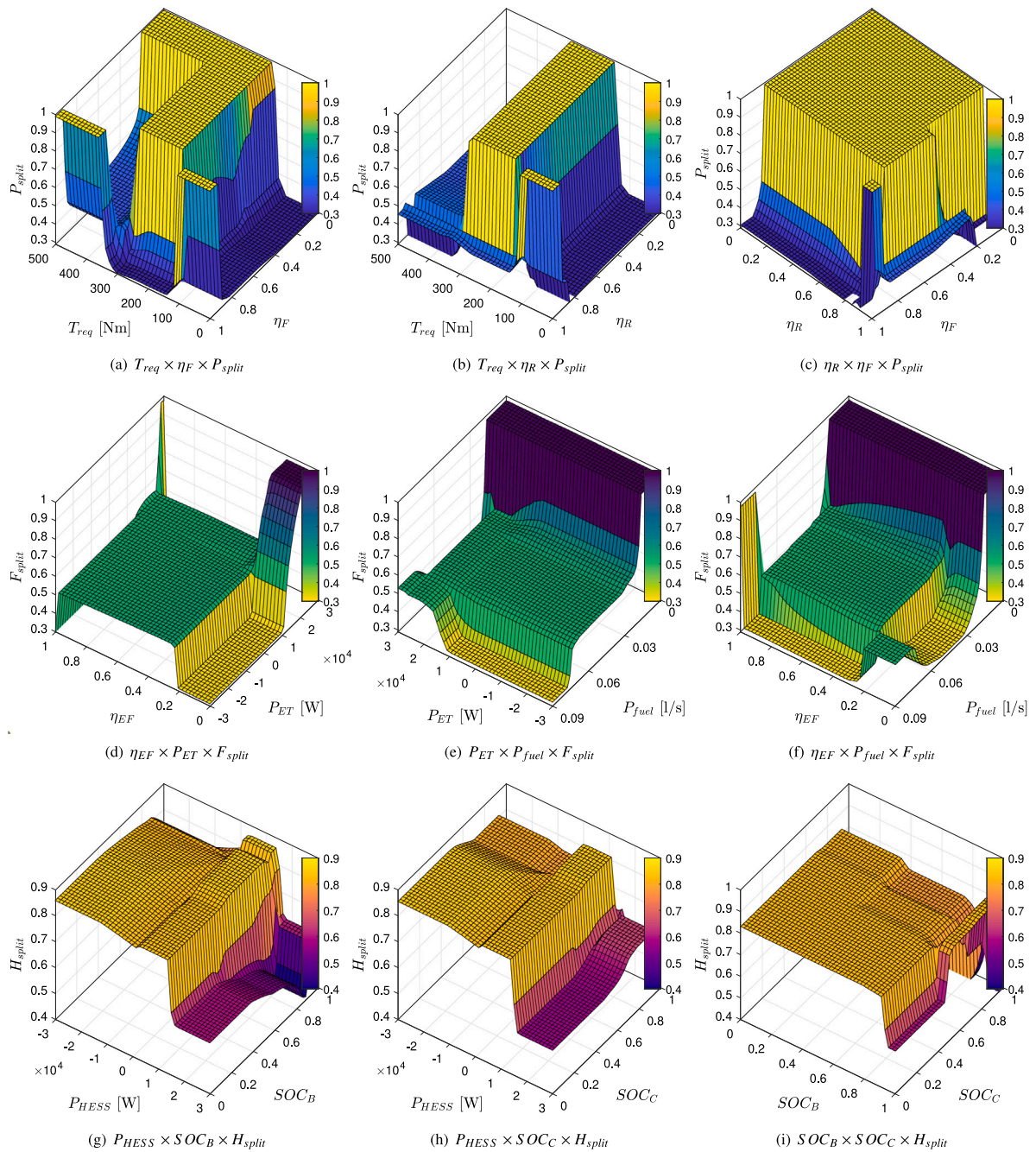**Fig. 9.** Simulation results for the best trade-off FCHEV configuration.

(a) $T_{req} \times \eta_F \times P_{split}$

(b) $T_{req} \times \eta_R \times P_{split}$

(c) $\eta_R \times \eta_F \times P_{split}$

(d) $\eta_{EF} \times P_{ET} \times F_{split}$

(e) $P_{ET} \times P_{fuel} \times F_{split}$

(f) $\eta_{EF} \times P_{fuel} \times F_{split}$

(g) $P_{HESS} \times SOC_B \times H_{split}$

(h) $P_{HESS} \times SOC_C \times H_{split}$

(i) $SOC_B \times SOC_C \times H_{split}$

Fig. 10. Best trade off fuzzy logic optimum controller surfaces.

Table 6
Cost comparison between optimal electrified vehicle powertrain configurations.

Parameters	FCHEV (current work)				
	$\max(f_1)$	$\min(f_2)$	$\min(f_3)$	$\min(f_4)$	$\max(Ft)$
Driving range [km]	461.96	400.41	95.15	422.23	444.08
Fuel cell cost	US$ 9000	US$ 9000	US$ 9000	US$ 9000	US$ 9000
Battery cost	US$ 2192	US$ 876	US$ 2158	US$ 1827	US$ 1534
Ultracapacitor cost	US$ 7277	US$ 1819	US$ 7277	US$ 10896	US$ 2079
Frontal EMs cost	US$ 1404	US$ 1005	US$ 1114	US$ 1060	US$ 1078
Rear EMs cost	US$ 232	US$ 367	US$ 197	US$ 245	US$ 202
Powertrain overall cost	US$ 20105	US$ 13067	US$ 19746	US$ 23028	US$ 13893
$\frac{\text{Overall cost}}{\text{Driving range}}$ [US$/km]	43.52	32.63	207.52	54.54	31.28
	Dual HESS-based EV [97]				
	$\max(D_R)$	$\min(M_{bat(F/R)} + M_{cap(F/R)})$	$\max(SoH_{(F/R)})$	$\min(f_4)$	$\max(Ft)$
Driving range [km]	369.16	98.34	223.98	– – –	285.56
Frontal battery cost	US$ 6673	US$ 1540	US$ 6294	– – –	US$ 5315
Frontal ultracapacitors cost	US$ 2339	US$ 1819	US$ 1819	– – –	US$ 1819
Frontal EMs cost	US$ 958	US$ 965	US$ 1124	– – –	US$ 1037
Rear battery cost	US$ 5964	US$ 706	US$ 2074	– – –	US$ 1871
Rear ultracapacitors cost	US$ 3358	US$ 1819	US$ 16933	– – –	US$ 1819
Rear EMs cost	US$ 728	US$ 320	US$ 399	– – –	US$ 303
Powertrain overall cost	US$ 20020	US$ 7169	US$ 28643	– – –	US$ 12164
$\frac{\text{Overall cost}}{\text{Driving range}}$ [US$/km]	54.23	72.90	127.88	– – –	42.60
	Single HESS-based EV [97]				
	$\max(D_R)$	$\min(M_{bat} + M_{cap})$	$\max(SoH)$	$\min(f_4)$	$\max(Ft)$
Driving range [km]	270.34	98.25	256.46	– – –	238.82
Battery cost	US$ 9019	US$ 2361	US$ 9140	– – –	US$ 6566
Ultracapacitor cost	US$ 1819	US$ 1819	US$ 1819	– – –	US$ 1819
Frontal EMs cost	US$ 1230	US$ 1120	US$ 1191	– – –	US$ 1136
Rear EMs cost	US$ 391	US$ 201	US$ 187	– – –	US$ 194
Powertrain overall cost	US$ 12459	US$ 5501	US$ 12337	– – –	US$ 9715
$\frac{\text{Overall cost}}{\text{Driving range}}$ [US$/km]	46.09	55.99	48.10	– – –	40.68
	Single battery EV [98]				
	$\min(\delta_{rms})$	$\max(SoC_B)$	$\min(M_{bat} + M_{EMs})$	$\min(f_4)$	$\max(Ft)$
Driving range [km]	88.5	152.40	80.70	– – –	124.20
Battery cost	US$ 5807	US$ 13620	US$ 4901	– – –	US$ 8030
Frontal EMs cost	US$ 1620	US$ 1898	US$ 1576	– – –	US$ 1364
Rear EMs cost	US$ 1187	US$ 1223	US$ 967	– – –	US$ 1279
Powertrain overall cost	US$ 8614	US$ 16741	US$ 7444	– – –	US$ 10673
$\frac{\text{Overall cost}}{\text{Driving range}}$ [US$/km]	97.33	109.85	92.24	– – –	85.93
	Electric-hydraulic hybrid vehicle EHHV [107]				
	$\max(D_R)$	$\min(M_{bat} + M_{hyd})$	$\max(SoH)$	$\min(f_4)$	$\max(Ft)$
Driving range [km]	199.73	104.04	148.51	– – –	167.95
Battery cost	US$ 9508	US$ 4828	US$ 7012	– – –	US$ 7925
EM cost	US$ 4279	US$ 4273	US$ 4287	– – –	US$ 4300
Hydraulic drivetrain cost	US$ 2076	US$ 2076	US$ 2076	– – –	US$ 2076
Powertrain overall cost	US$ 15863	US$ 11177	US$ 13375	– – –	US$ 14301
$\frac{\text{Overall cost}}{\text{Driving range}}$ [US$/km]	79.42	107.43	90.06	– – –	85.15

explained by the fact that this configuration primarily focused on the reduction of hydrogen consumption by the increase of the HESS size, which increases the cost of ownership without reflecting in a proper increase of driving range. In fact, $\min(f_3)$ solution used only 0.58 kg of hydrogen fuel, which is a considerably lower value when compared to those of other optimal configurations that used the total amount of fuel stored in the tank (4 kg). As a result, $\min(f_3)$ configuration achieved an approximate 95 km range, which corresponds to only 23% of the driving range accomplished by the best trade-off configuration. Thus, it is possible to infer that the $\min(f_3)$ solution presents a relevant increase in the total cost of ownership per driving range, as an expensive investment on a fuel cell system is made, but it is only used in short routes during the cycle, while the HESS is prioritized and utilized as the main power source. At the same time, $\min(f_3)$ can be seen as a beneficial configuration in terms of operating costs, as the hydrogen fuel efficiency is increased by up to 38.71% as compared to the most compromised configuration ($\max(F_t)$).

5.2. Alternative driving cycles

Another important factor that should be evaluated is the robustness of the optimal FCHEV configurations with regard to other driving profiles. Hence, this subsection presents the results of the optimized solutions under real-world driving cycles at urban scenarios from the Brazilian cities of Ouro Branco (Minas Gerais) [110], Campinas (São Paulo state) [67], and Santa Maria (Rio Grande do Sul) [112,113]. Additionally, those configurations were also subjected to the highway route from Campinas to São Paulo city [98].

Table 7 shows that most of the optimal configurations achieved driving autonomy greater than the minimum range established by the optimization constraint ($D_R \geq 94$ km). The only exception was the $\min(f_3)$ solution under the Campinas-to-São Paulo driving cycle, presenting 81.01 km of autonomy. This can be explained by the fact that this real-world cycle consists of a highway profile that demands more power when compared against the urban cycles described in this

Table 7
Optimized results under alternative driving cycles.

Results	FCHEV solutions				
	Maximum driving range max(f_1)	Minimum HESS mass min(f_2)	Minimum H_2 consumption min(f_3)	Longest life cycle min(f_4)	Best trade-off max(Ft)
Ouro Branco driving cycle [110]					
H_2 consumption [kg/100 km]	0.6319	0.8003	0.6074	0.7882	0.7072
Driving range [km]	633.16	499.81	194.49	499.14	565.62
Performance COR	0.9999	0.9999	0.9997	0.9999	0.9999
SoH	0.9978	0.9973	0.9896	0.9973	0.9984
FC voltage drop V_{drop} [µV/h]	3.50	3.52	5.12	3.34	3.34
FC lifespan L_{fc} [h]	10861	10811	7423	11381	11386
Santa Maria driving cycle [112,113]					
H_2 consumption [kg/100 km]	0.5601	0.7992	0.7104	0.7946	0.7068
Driving range [km]	714.24	500.51	333.67	481.85	565.98
Performance COR	1.0000	1.0000	1.0000	1.0000	1.0000
SoH	0.9991	0.9980	0.9962	0.9990	0.9984
FC voltage drop V_{drop} [µV/h]	3.48	3.35	3.55	3.23	3.31
FC lifespan L_{fc} [h]	10915	11342	10718	11759	11505
Campinas to São Paulo driving cycle [98]					
H_2 consumption [kg/100 km]	0.9297	1.1741	0.5434	1.0616	1.0329
Driving range [km]	430.32	279.27	81.01	376.82	363.19
Performance COR	0.9999	0.9954	0.9971	0.9961	0.9964
SoH	0.9972	0.9997	0.9977	0.9977	0.9960
FC voltage drop V_{drop} [µV/h]	6.09	5.01	13.42	4.77	4.27
FC lifespan L_{fc} [h]	6234	7589	2834	7968	8901
Campinas driving cycle [67]					
H_2 consumption [kg/100 km]	0.6697	0.8899	0.7196	0.8815	0.8012
Driving range [km]	597.45	449.53	190.77	447.73	499.31
Performance COR	0.9999	0.9999	0.9997	0.9998	0.9998
SoH	0.9988	0.9989	0.9956	0.9990	0.9988
FC voltage drop V_{drop} [µV/h]	4.91	4.87	5.53	4.71	4.78
FC lifespan L_{fc} [h]	7757	7798	6876	8060	7963

section. In addition, it is important to emphasize that Campinas-to-São Paulo cycle presents fewer significant deceleration routes, which affects the energy braking regeneration of the ultracapacitor. As a result, this cycle also requires, in most cases, more hydrogen fuel than those of the Ouro Branco, Santa Maria, and Campinas driving cycles.

Santa Maria cycle provides the highest driving range for the optimized solutions. As an urban driving scenario that presents driving profiles of heavy traffic and free road with relatively low speed and power demand, the FCHEV configurations were able to achieve a higher energy regeneration and efficiency.

The simulation results for the Campinas and Ouro Branco driving cycles also presented high driving autonomy. The best trade-off solution, for instance, achieved a lower hydrogen fuel consumption (−11.06% for the Campinas and −21.51% for the Ouro Branco cycle) as compared to that of the combined standardized cycle in which the optimization method was employed. Analogously to the Santa Maria cycle, those cycles are characterized by urban driving routes combined by low-speed traffic conditions, in which regenerative braking can easily occur. Regarding the degradation of the power sources, there is a clear tendency of shorter fuel cell life cycles for the configurations under the Campinas-to-São Paulo cycle when compared to the aforementioned real-world urban driving profiles.

As can be observed by the provided results, it is possible to infer that the optimal FCHEV configurations presented robustness under real-world driving profiles, distinct from the ones used in the formulation of the i-AWGA method, not only with respect to energy efficiency and autonomy, but also regarding performance and power sources life cycle. In this sense, the most compromised solution (max(Ft)) managed to best balance all the optimization targets under different driving conditions and can be considered, therefore, the most robust configurations achieved in this work.

6. Conclusion

In this study, a multi-objective optimization procedure is employed for the power management control and design of a fuel cell hybrid electric vehicle (FCHEV) powertrain architecture equipped with a battery-ultracapacitor HESS. The formulation of the optimization problem is based on the i-AWGA method and targets the maximization of driving autonomy and power sources lifetime expectancy, while also minimizing hydrogen fuel consumption and HESS size. Fuzzy controllers' parameters and design variables are considered in such formulation, which is subjected to the necessary optimization constraints.

The optimization results of this work justify the choice for a HESS-based FCHEV powertrain topology along with an efficient aging-aware energy management strategy. Among the non-dominated solutions in the Pareto frontier, the best trade-off configuration (that is, the most compromised solution regarding the optimization criteria) achieved a driving autonomy of 444 km and up to 714 km for the combined standard cycle and real-world driving profiles, respectively. This optimized solution also presented hydrogen consumption in the range of 0.7072 to 0.9009 kg/100 km, for all driving conditions analyzed in this study, while keeping good vehicle performance and suitable lifetime of the power sources (fuel cell and battery).

Moreover, cost–benefit analysis was carried out in this work, in which the optimal FCHEV configuration was compared to other electrified powertrain topologies with respect to their costs of ownership. The max(Ft) solution obtained a significant reduction in the cost-to-autonomy ratio of 63.59%, 23.11%, 26.57%, and 63.26% as compared to the optimized EV, single HESS-based EV, dual HESS-based EV, and EHHV, respectively.

Nevertheless, it is noteworthy to highlight that important drawbacks such as expensive maintenance, high hydrogen fuel price, and lack of

infrastructure and logistics to supply hydrogen gas stations at large scale should be investigated and addressed in order to accelerate the adoption of fuel cell propulsion systems in the automotive industry.

As future works, machine learning models will be used as a potential alternative for the energy management of electrically propelled vehicles. Additionally, other powertrain architectures that combine multiple power sources will be evaluated in terms of energy efficiency, autonomy and lifespan of the energy storage systems.

CRediT authorship contribution statement

Samuel Filgueira da Silva: Conceptualization, Methodology, Software, Investigation, Formal analysis, Validation, Data curation, Writing – original draft, Writing – review & editing, Visualization. **Jony Javorski Eckert:** Conceptualization, Methodology, Software, Investigation, Formal analysis, Validation, Data curation, Writing – original draft, Writing – review & editing, Visualization. **Fabrício Leonardo Silva:** Conceptualization, Methodology, Software, Writing – review & editing, Visualization. **Fernanda Cristina Corrêa:** Conceptualization, Methodology, Software, Writing – review & editing, Visualization. **Ludmila C.A. Silva:** Resources, Writing – review & editing, Supervision, Funding acquisition, Project administration. **André Valente Bueno:** Resources, Conceptualization, Methodology, Software, Writing – review & editing, Visualization, Funding acquisition, Project administration. **Franco Giuseppe Dedini:** Resources, Writing – review & editing, Supervision.

Declaration of competing interest

The authors declare that they have no known competing financial interests or personal relationships that could have appeared to influence the work reported in this paper.

Data availability

No data was used for the research described in the article.

Acknowledgments

References

[1] Rafaj P, Kiesewetter G, Gül T, Schöpp W, Cofala J, Klimont Z, et al. Outlook for clean air in the context of sustainable development goals. Global Environ Change 2018;53:1–11. http://dx.doi.org/10.1016/j.gloenvcha.2018.08.008.

[2] Mace MJ. Mitigation commitments under the Paris agreement and the way forward. Clim Law 2016;6(1–2):21–39. http://dx.doi.org/10.1163/18786561-00601002.

[3] Horowitz CA. Paris agreement. Int Leg Mater 2016;55(4):740–55.

[4] Sikora A. European Green Deal–legal and financial challenges of the climate change. In: ERA forum, vol. 21, no. 4. Springer; 2021, p. 681–97. http://dx.doi.org/10.1007/s12027-020-00637-3.

[5] Organisation for Economic Co-Operation and Development. Energy technology perspectives 2017: Catalysing energy technology transformations. Technical report, International Energy Agency; 2017.

[6] Frey HC. Trends on onroad transportation energy and emissions. J Air Waste Manage Assoc 2018;68(6):514–63. http://dx.doi.org/10.1080/10962247.2018.1454357.

[7] Cano ZP, Banham D, Ye S, Hintennach A, Lu J, Fowler M, et al. Batteries and fuel cells for emerging electric vehicle markets. Nat Energy 2018;3(4):279–89. http://dx.doi.org/10.1038/s41560-018-0108-1.

[8] Wappelhorst S. The end of the road? An overview of combustion-engine car phase-out announcements across Europe. Briefing. Int Counc Clean Transp 2020.

[9] Morfeldt J, Davidsson Kurland S, Johansson DJ. Carbon footprint impacts of banning cars with internal combustion engines. Transp Res D 2021;95:102807. http://dx.doi.org/10.1016/j.trd.2021.102807.

[10] Corno M, Pozzato G. Active adaptive battery aging management for electric vehicles. IEEE Trans Veh Technol 2020;69(1):258–69. http://dx.doi.org/10.1109/TVT.2019.2940033.

[11] Sierzchula W, Bakker S, Maat K, van Wee B. The influence of financial incentives and other socio-economic factors on electric vehicle adoption. Energy Policy 2014;68:183–94. http://dx.doi.org/10.1016/j.enpol.2014.01.043.

[12] Hill G, Heidrich O, Creutzig F, Blythe P. The role of electric vehicles in near-term mitigation pathways and achieving the UK's carbon budget. Appl Energy 2019;251:113111. http://dx.doi.org/10.1016/j.apenergy.2019.04.107.

[13] Dhar S, Pathak M, Shukla PR. Electric vehicles and India's low carbon passenger transport: a long-term co-benefits assessment. J Clean Prod 2017;146:139–48. http://dx.doi.org/10.1016/j.jclepro.2016.05.111, Bridging the Gaps for Accelerating Low Carbon Actions in Asia.

[14] Linn J, McConnell V. Interactions between federal and state policies for reducing vehicle emissions. Energy Policy 2019;126:507–17. http://dx.doi.org/10.1016/j.enpol.2018.10.052.

[15] Sidharthan Panaparambil V, Kashyap Y, Vijay Castelino R. A review on hybrid source energy management strategies for electric vehicle. Int J Energy Res 2021;1–32. http://dx.doi.org/10.1002/er.7107.

[16] Yu H, Dezza FC, Cheli F, Tang X, Hu X, Lin X. Dimensioning and power management of hybrid energy storage systems for electric vehicles with multiple optimization criteria. IEEE Trans Power Electron 2020. http://dx.doi.org/10.1109/TPEL.2020.3030822.

[17] Zhang Z, Zhang T, Hong J, Zhang H, Yang J. Energy management strategy of a novel parallel electric-hydraulic hybrid electric vehicle based on deep reinforcement learning and entropy evaluation. J Clean Prod 2023;403:136800. http://dx.doi.org/10.1016/j.jclepro.2023.136800.

[18] Kumar L, Jain S. Electric propulsion system for electric vehicular technology: A review. Renew Sustain Energy Rev 2014;29:924–40. http://dx.doi.org/10.1016/j.rser.2013.09.014.

[19] Barbosa TP, Eckert JJ, Roso VR, Pacheco Pujatti FJ, Rodrigues da Silva LA, Horta Gutiérrez JC. Fuel saving and lower pollutants emissions using an Ethanol-fueled engine in a hydraulic hybrid passengers vehicle. Energy 2021;235:121361. http://dx.doi.org/10.1016/j.energy.2021.121361.

[20] Knupfer SM, Hensley R, Hertzke P, Schaufuss P, Laverty N, Kramer N. Electrifying insights: How automakers can drive electrified vehicle sales and profitability. McKinsey & Company; 2017.

[21] Fallah N, Fitzpatrick C, Killian S, Johnson M. End-of-life electric vehicle battery stock estimation in Ireland through integrated energy and circular economy modelling. Resour Conserv Recy 2021;174:105753. http://dx.doi.org/10.1016/j.resconrec.2021.105753.

[22] Woody M, Arbabzadeh M, Lewis GM, Keoleian GA, Stefanopoulou A. Strategies to limit degradation and maximize li-ion battery service lifetime - critical review and guidance for stakeholders. J Energy Storage 2020;28:101231. http://dx.doi.org/10.1016/j.est.2020.101231.

[23] De Pascali L, Biral F, Onori S. Aging-aware optimal energy management control for a parallel hybrid vehicle based on electrochemical-degradation dynamics. IEEE Trans Veh Technol 2020;69(10):10868–78. http://dx.doi.org/10.1109/TVT.2020.3019241.

[24] Zhang S, Xiong R. HESS and its application in series hybrid electric vehicles. In: Modeling, dynamics and control of electrified vehicles. Elsevier; 2018, p. 77–119. http://dx.doi.org/10.1016/B978-0-12-812786-5.00003-3.

[25] Power split strategies for hybrid energy storage systems for vehicular applications. J Power Sources 2014;258:395–407. http://dx.doi.org/10.1016/j.jpowsour.2014.01.118.

[26] Zhang S, Xiong R, Cao J. Battery durability and longevity based power management for plug-in hybrid electric vehicle with hybrid energy storage system. Appl Energy 2016;179:316–28. http://dx.doi.org/10.1016/j.apenergy.2016.06.153.

[27] Zhang L, Hu X, Wang Z, Sun F, Deng J, Dorrell DG. Multiobjective optimal sizing of hybrid energy storage system for electric vehicles. IEEE Trans Veh Technol 2017;67(2):1027–35. http://dx.doi.org/10.1109/TVT.2017.2762368.

[28] Choi M-E, Lee J-S, Seo S-W. Real-time optimization for power management systems of a battery/supercapacitor hybrid energy storage system in electric vehicles. IEEE Trans Veh Technol 2014;63(8):3600–11. http://dx.doi.org/10.1109/TVT.2014.2305593.

[29] Corbo P, Migliardini F, Veneri O. Hydrogen fuel cells for road vehicles. Springer Science & Business Media; 2011.

[30] Ade N, Wilhite B, Goyette H, Mannan MS. Intensifying vehicular proton exchange membrane fuel cells for safer and durable, design and operation. Int J Hydrogen Energy 2020;45(7):5039–54. http://dx.doi.org/10.1016/j.ijhydene.2019.12.011.

[31] Franco AA. Polymer electrolyte fuel cells: Science, applications, and challenges. CRC Press; 2013.

[32] Erjavec J. Hybrid, electric, and fuel-cell vehicles. Cengage Learning; 2012.

[33] Scrosati B, Garche J, Tillmetz W. Advances in battery technologies for electric vehicles. Woodhead Publishing; 2015, http://dx.doi.org/10.1016/C2014-0-02665-2.

[34] El-Shafie M, Kambara S, Hayakawa Y, et al. Hydrogen production technologies overview. J Power Energy Eng 2019;7(01):107. http://dx.doi.org/10.4236/jpee.2019.71007.

[35] Dincer I, Acar C. Smart energy solutions with hydrogen options. Int J Hydrogen Energy 2018;43(18):8579–99. http://dx.doi.org/10.1016/j.ijhydene.2018.03.120.

[36] Dincer I, Acar C. Review and evaluation of hydrogen production methods for better sustainability. Int J Hydrogen Energy 2015;40(34):11094–111. http://dx.doi.org/10.1016/j.ijhydene.2014.12.035.

[37] Tanaka S, Nagumo K, Yamamoto M, Chiba H, Yoshida K, Okano R. Fuel cell system for Honda CLARITY fuel cell. eTransportation 2020;3:100046. http://dx.doi.org/10.1016/j.etran.2020.100046.

[38] Pielecha I, Cieślik W, Szałek A. The use of electric drive in urban driving conditions using a hydrogen powered vehicle-Toyota Mirai. Combust Engines 2018;57. http://dx.doi.org/10.19206/CE-2018-106.

[39] Lohse-Busch H, Stutenberg K, Duoba M, Iliev S. Technology assessment of a fuel cell vehicle: 2017 Toyota Mirai. Tech. rep., Argonne, IL (United States): Argonne National Lab.(ANL); 2018.

[40] Hong BK, Kim SH. (Invited) Recent advances in fuel cell electric vehicle technologies of Hyundai. ECS Trans 2018;86(13):3–11. http://dx.doi.org/10.1149/08613.0003ecst.

[41] Nissan unveils world's first FCEV with SOFC running on bioethanol. Fuel Cells Bull 2016;2016(9):3. http://dx.doi.org/10.1016/S1464-2859(16)30231-0.

[42] Ma S, Lin M, Lin T-E, Lan T, Liao X, Maréchal F, et al. Fuel cell-battery hybrid systems for mobility and off-grid applications: A review. Renew Sustain Energy Rev 2021;135:110119. http://dx.doi.org/10.1016/j.rser.2020.110119.

[43] Jablonski J, Hackenberg-Wiedl P, Rank S. AUDI h-tron – A key-technology to meeting the requirements for sustainable drive concepts. In: Bargende M, Reuss H-C, Wiedemann J, editors. 18. Internationales stuttgarter symposium. Wiesbaden: Springer Fachmedien Wiesbaden; 2018, p. 225–31. http://dx.doi.org/10.1007/978-3-658-21194-3_20.

[44] Venturi M, Mohrdieck C, Friedrich J. Mercedes-Benz B-Class Fuel Cell: The world largest hydrogen vehicle fuel cell fleet experience. In: 2013 World electric vehicle symposium and exhibition. 2013, p. 1–11. http://dx.doi.org/10.1109/EVS.2013.6915019.

[45] Mohrdieck C, Dehn S. The intelligent fuel cell plug-in hybrid drive system of the Mercedes-Benz GLC F-cell. MTZ Worldw 2019;80(1):30–7. http://dx.doi.org/10.1007/s38313-018-0121-6.

[46] Zhou Y, Ravey A, Péra M-C. Real-time cost-minimization power-allocating strategy via model predictive control for fuel cell hybrid electric vehicles. Energy Convers Manage 2021;229:113721. http://dx.doi.org/10.1016/j.enconman.2020.113721.

[47] Ravey A, Blunier B, Miraoui A. Control strategies for fuel-cell-based hybrid electric vehicles: From offline to online and experimental results. IEEE Trans Veh Technol 2012;61(6):2452–7. http://dx.doi.org/10.1109/TVT.2012.2198680.

[48] Energy control strategies for the Fuel Cell Hybrid Power Source under unknown load profile. Energy 2015;86:31–41. http://dx.doi.org/10.1016/j.energy.2015.03.118.

[49] Zhou Y, Ravey A, Péra M-C. Multi-mode predictive energy management for fuel cell hybrid electric vehicles using Markov driving pattern recognizer. Appl Energy 2020;258:114057. http://dx.doi.org/10.1016/j.apenergy.2019.114057.

[50] Optimal economy-based battery degradation management dynamics for fuel-cell plug-in hybrid electric vehicles. J Power Sources 2015;274:367–81. http://dx.doi.org/10.1016/j.jpowsour.2014.10.011.

[51] Nie Z, Jia Y, Wang W, Lian Y, Outbib R. Co-optimization strategies for connected and automated fuel cell hybrid vehicles in dynamic curving scenarios. Int J Hydrogen Energy 2023;48(8):3252–68. http://dx.doi.org/10.1016/j.ijhydene.2022.10.161.

[52] Li H, Ravey A, N'Diaye A, Djerdir A. Online adaptive equivalent consumption minimization strategy for fuel cell hybrid electric vehicle considering power sources degradation. Energy Convers Manage 2019;192:133–49. http://dx.doi.org/10.1016/j.enconman.2019.03.090.

[53] An energy management strategy to concurrently optimise fuel consumption & PEM fuel cell lifetime in a hybrid vehicle. Int J Hydrogen Energy 2016;41(46):21503–15. http://dx.doi.org/10.1016/j.ijhydene.2016.08.157.

[54] Towards health-aware energy management strategies in fuel cell hybrid electric vehicles: A review. Int J Hydrogen Energy 2022;47(17):10021–43. http://dx.doi.org/10.1016/j.ijhydene.2022.01.064.

[55] Hu X, Johannesson L, Murgovski N, Egardt B. Longevity-conscious dimensioning and power management of the hybrid energy storage system in a fuel cell hybrid electric bus. Appl Energy 2015;137:913–24. http://dx.doi.org/10.1016/j.apenergy.2014.05.013.

[56] Wang Y, Moura SJ, Advani SG, Prasad AK. Power management system for a fuel cell/battery hybrid vehicle incorporating fuel cell and battery degradation. Int J Hydrogen Energy 2019;44(16):8479–92. http://dx.doi.org/10.1016/j.ijhydene.2019.02.003.

[57] Khan MS, Ahmad I, Armaghan H, Ali N. Backstepping sliding mode control of FC-UC based hybrid electric vehicle. IEEE Access 2018;6:77202–11. http://dx.doi.org/10.1109/ACCESS.2018.2879881.

[58] Rahman AU, Zehra SS, Ahmad I, Armghan H. Fuzzy supertwisting sliding mode-based energy management and control of hybrid energy storage system in electric vehicle considering fuel economy. J Energy Storage 2021;37:102468. http://dx.doi.org/10.1016/j.est.2021.102468.

[59] Mohammed AS, Atnaw SM, Salau AO, Eneh JN. Review of optimal sizing and power management strategies for fuel cell/battery/super capacitor hybrid electric vehicles. Energy Rep 2023;9:2213–28. http://dx.doi.org/10.1016/j.egyr.2023.01.042.

[60] Gillespie TD. Fundamentals of vehicle dynamics. Society of Automotive Engineers - SAE; 1992.

[61] Eckert JJ, Silva LCdA, Dedini FG, Corrêa FC. Electric vehicle powertrain and fuzzy control multi-objective optimization, considering dual hybrid energy storage systems. IEEE Trans Veh Technol 2020;69(4):3773–82. http://dx.doi.org/10.1109/TVT.2020.2973601.

[62] Eckert JJ, Silva LC, Costa ES, Santiciolli FM, Dedini FG, Corrêa FC. Electric vehicle drivetrain optimisation. IET Electr Syst Transp 2017;7(1):32–40. http://dx.doi.org/10.1049/iet-est.2016.0022.

[63] Cao J, Emadi A. A new battery/ultracapacitor hybrid energy storage system for electric, hybrid, and plug-in hybrid electric vehicles. IEEE Trans Power Electron 2011;27(1):122–32.

[64] Song Z, Hofmann H, Li J, Hou J, Han X, Ouyang M. Energy management strategies comparison for electric vehicles with hybrid energy storage system. Appl Energy 2014;134:321–31. http://dx.doi.org/10.1016/j.apenergy.2014.08.035.

[65] Geetha A, Subramani C. A comprehensive review on energy management strategies of hybrid energy storage system for electric vehicles. Int J Energy Res 2017;41(13):1817–34.

[66] Seixas LD, Tosso HG, Corrêa FC, Eckert JJ. Particle swarm optimization of a fuzzy controlled hybrid energy storage system - HESS. In: 2020 IEEE vehicle power and propulsion conference. 2020, p. 1–6. http://dx.doi.org/10.1109/VPPC49601.2020.9330939.

[67] Eckert JJ, da Silva SF, de Menezes Lourenço MA, Corrêa FC, Silva LC, Dedini FG. Energy management and gear shifting control for a hybridized vehicle to minimize gas emissions, energy consumption and battery aging. Energy Convers Manage 2021;240:114222. http://dx.doi.org/10.1016/j.enconman.2021.114222.

[68] Tong W. Mechanical design of electric motors. CRC Press; 2014.

[69] Yamashita RY, Silva FL, Santiciolli FM, Eckert JJ, Dedini FG, Silva LC. Comparison between two models of BLDC motor, simulation and data acquisition. J Braz Soc Mech Sci Eng 2018;40(2):1–11. http://dx.doi.org/10.1007/s40430-018-1020-0.

[70] Huang Y, Surawski NC, Organ B, Zhou JL, Tang OH, Chan EF. Fuel consumption and emissions performance under real driving: Comparison between hybrid and conventional vehicles. Sci Total Environ 2019;659:275–82. http://dx.doi.org/10.1016/j.scitotenv.2018.12.349.

[71] Eckert JJ, Silva LCdAe, Costa EdS, Santiciolli FM, Corrêa FC, Dedini FG. Optimization of electric propulsion system for a hybridized vehicle. Mech Based Des Struct Mach 2019;47(2):175–200. http://dx.doi.org/10.1080/15397734.2018.1520129.

[72] Thackeray MM, Wolverton C, Isaacs ED. Electrical energy storage for transportation—approaching the limits of, and going beyond, lithium-ion batteries. Energy Environ Sci 2012;5(7):7854–63. http://dx.doi.org/10.1039/C2EE21892E.

[73] Wang C-Y, Zhang G, Ge S, Xu T, Ji Y, Yang X-G, et al. Lithium-ion battery structure that self-heats at low temperatures. Nature 2016;529(7587):515–8. http://dx.doi.org/10.1038/nature16502.

[74] Motapon SN, Lachance E, Dessaint L-A, Al-Haddad K. A generic cycle life model for lithium-ion batteries based on fatigue theory and equivalent cycle counting. IEEE Open J Ind Electron Soc 2020;1:207–17. http://dx.doi.org/10.1109/OJIES.2020.3015396.

[75] Zhang L, Hu X, Wang Z, Sun F, Dorrell DG. A review of supercapacitor modeling, estimation, and applications: A control/management perspective. Renew Sustain Energy Rev 2018;81:1868–78. http://dx.doi.org/10.1016/j.rser.2017.05.283.

[76] ISO. Electrically propelled road vehicles - Test specification for lithium-ion traction battery packs and systems - Part 2: High-energy applications, ISO Standard No.12405-2:2012, pp. 1–60.

[77] Motapon SN, Tremblay O, Dessaint L-A. Development of a generic fuel cell model: application to a fuel cell vehicle simulation. Int J Power Electron 2012;4(6):505–22. http://dx.doi.org/10.1504/IJPELEC.2012.052427.

[78] Larminie J, Dicks A, McDonald MS. Fuel cell systems explained, vol. 2. J. Wiley Chichester, UK; 2003.

[79] Ballard Power Systems Inc. Product data sheet. 2022, https://www.ballard.com/.

[80] Chen H, Pei P, Song M. Lifetime prediction and the economic lifetime of Proton Exchange Membrane fuel cells. Appl Energy 2015;142:154–63. http://dx.doi.org/10.1016/j.apenergy.2014.12.062.

[81] Chen D, Pei P, Meng Y, Ren P, Li Y, Wang M, et al. Novel extraction method of working condition spectrum for the lifetime prediction and energy management strategy evaluation of automotive fuel cells. Energy 2022;255:124523. http://dx.doi.org/10.1016/j.energy.2022.124523.

[82] Feng Y, Liu Q, Li Y, Yang J, Dong Z. Energy efficiency and CO2 emission comparison of alternative powertrain solutions for mining haul truck using integrated design and control optimization. J Clean Prod 2022;370:133568. http://dx.doi.org/10.1016/j.jclepro.2022.133568.

[83] Pei P, Chang Q, Tang T. A quick evaluating method for automotive fuel cell lifetime. Int J Hydrogen Energy 2008;33(14):3829–36. http://dx.doi.org/10.1016/j.ijhydene.2008.04.048, TMS07: Symposium on Materials in Clean Power Systems.

[84] Guenounou O, Dahhou B, Chabour F. Adaptive fuzzy controller based MPPT for photovoltaic systems. Energy Convers Manage 2014;78:843–50. http://dx.doi.org/10.1016/j.enconman.2013.07.093.

[85] Long S, Geng S. Decision framework of photovoltaic module selection under interval-valued intuitionistic fuzzy environment. Energy Convers Manage 2015;106:1242–50. http://dx.doi.org/10.1016/j.enconman.2015.10.037.

[86] Beddar A, Bouzekri H, Babes B, Afghoul H. Experimental enhancement of fuzzy fractional order PI+I controller of grid connected variable speed wind energy conversion system. Energy Convers Manage 2016;123:569–80. http://dx.doi.org/10.1016/j.enconman.2016.06.070.

[87] Li E-H, Li Y-Z, Xie J-Y, Sun Y-H, Yang L-Z, Ning X-W. A fuzzy coordination control of a water membrane evaporator cooling system for aerospace electronics. Appl Therm Eng 2021;191:116872. http://dx.doi.org/10.1016/j.applthermaleng.2021.116872.

[88] Dong S-J, Li Y-Z, Wang J, Wang J. Fuzzy incremental control algorithm of loop heat pipe cooling system for spacecraft applications. Comput Math Appl 2012;64(5):877–86. http://dx.doi.org/10.1016/j.camwa.2012.01.030, Advanced Technologies in Computer, Consumer and Control.

[89] Teodorescu H-NL, Kandel A, Jain LC. Fuzzy logic and neuro-fuzzy systems in medicine and bio-medical engineering: a historical perspective. In: Fuzzy and neuro-fuzzy systems in medicine. CRC Press; 2017, p. 1–18.

[90] Mahmoudi SM, Maleki A, Rezaei Ochbelagh D. Optimization of a hybrid energy system with/without considering back-up system by a new technique based on fuzzy logic controller. Energy Convers Manage 2021;229:113723. http://dx.doi.org/10.1016/j.enconman.2020.113723.

[91] Sahu A, Patel US. Modelling & simulation of fuzzy logic based controller for energy storage system. J Electron Des Technol 2017;8(2):9–15.

[92] Herrera V, Milo A, Gaztañaga H, Etxeberria-Otadui I, Villarreal I, Camblong H. Adaptive energy management strategy and optimal sizing applied on a battery-supercapacitor based tramway. Appl Energy 2016;169:831–45. http://dx.doi.org/10.1016/j.apenergy.2016.02.079.

[93] Li P, Jiao X, Li Y. Adaptive real-time energy management control strategy based on fuzzy inference system for plug-in hybrid electric vehicles. Control Eng Pract 2021;107:104703. http://dx.doi.org/10.1016/j.conengprac.2020.104703.

[94] Yang C, Liu K, Jiao X, Wang W, Chen R, You S. An adaptive firework algorithm optimization-based intelligent energy management strategy for plug-in hybrid electric vehicles. Energy 2021;122120. http://dx.doi.org/10.1016/j.energy.2021.122120.

[95] Shi D, Liu S, Cai Y, Wang S, Li H, Chen L. Pontryagin's minimum principle based fuzzy adaptive energy management for hybrid electric vehicle using real-time traffic information. Appl Energy 2021;286:116467. http://dx.doi.org/10.1016/j.apenergy.2021.116467.

[96] Eckert JJ, Silva FL, da Silva SF, Bueno AV, de Oliveira MLM, Silva LC. Optimal design and power management control of hybrid biofuel–electric powertrain. Appl Energy 2022;325:119903. http://dx.doi.org/10.1016/j.apenergy.2022.119903.

[97] da Silva SF, Eckert JJ, Corrêa FC, Silva FL, Silva LC, Dedini FG. Dual HESS electric vehicle powertrain design and fuzzy control based on multi-objective optimization to increase driving range and battery life cycle. Appl Energy 2022;324:119723. http://dx.doi.org/10.1016/j.apenergy.2022.119723.

[98] Miranda MH, Silva FL, Lourenço MA, Eckert JJ, Silva LC. Electric vehicle powertrain and fuzzy controller optimization using a planar dynamics simulation based on a real-world driving cycle. Energy 2021;121979. http://dx.doi.org/10.1016/j.energy.2021.121979.

[99] Silva FL, Silva LC, Eckert JJ, de Menezes Lourenço MA. Robust fuzzy stability control optimization by multi-objective for modular vehicle. Mech Mach Theory 2022;167:104554. http://dx.doi.org/10.1016/j.mechmachtheory.2021.104554.

[100] Silva FL, da Silva SF, Mazzariol FS, Eckert JJ, Silva LCA, Dedini FG. Multi-objective optimization of the steering system and fuzzy logic control applied to a car-like robot. In: Multibody mechatronic systems. Cham: Springer International Publishing; 2021, p. 195–202. http://dx.doi.org/10.1007/978-3-030-60372-4_22.

[101] Wang S, Liu Y, Wang Z, Dong P, Cheng Y, Xu X, et al. Adaptive fuzzy iterative control strategy for the wet-clutch filling of automatic transmission. Mech Syst Signal Process 2019;130:164–82. http://dx.doi.org/10.1016/j.ymssp.2019.05.008.

[102] Eckert J, Santiciolli F, Yamashita R, Correa F, Silva LC, Dedini F. Fuzzy gear shifting control optimization to improve vehicle performance, fuel consumption and engine emissions. IET Control Theory Appl 2019. http://dx.doi.org/10.1049/iet-cta.2018.6272.

[103] Çeven S, Albayrak A, Bayır R. Real-time range estimation in electric vehicles using fuzzy logic classifier. Comput Electr Eng 2020;83:106577. http://dx.doi.org/10.1016/j.compeleceng.2020.106577.

[104] Mahmoud M. Fuzzy control, estimation and diagnosis: Single and interconnected systems. 2018, http://dx.doi.org/10.1007/978-3-319-54954-5.

[105] da Silva SF, Eckert JJ, Silva FL, Silva LC, Dedini FG. Multi-objective optimization design and control of plug-in hybrid electric vehicle powertrain for minimization of energy consumption, exhaust emissions and battery degradation. Energy Convers Manage 2021;234:113909. http://dx.doi.org/10.1016/j.enconman.2021.113909.

[106] Gen M, Cheng R, Lin L. Network models and optimization: Multiobjective genetic algorithm approach. Springer Science & Business Media; 2008.

[107] Eckert JJ, Barbosa TP, da Silva SF, Silva FL, Silva LC, Dedini FG. Electric hydraulic hybrid vehicle powertrain design and optimization-based power distribution control to extend driving range and battery life cycle. Energy Convers Manage 2022;252:115094. http://dx.doi.org/10.1016/j.enconman.2021.115094.

[108] Eckert JJ, Santiciolli FM, Silva LCA, Dedini FG. Vehicle drivetrain design multi-objective optimization. Mech Mach Theory 2021;156(1). http://dx.doi.org/10.1016/j.mechmachtheory.2020.104123.

[109] Eckert JJ, da Silva SF, Santiciolli FM, de Carvalho AC, Dedini FG. Multi-speed gearbox design and shifting control optimization to minimize fuel consumption, exhaust emissions and drivetrain mechanical losses. Mech Mach Theory 2022;169:104644. http://dx.doi.org/10.1016/j.mechmachtheory.2021.104644.

[110] Barbosa TP, Eckert JJ, Silva LCA, da Silva LAR, Gutiérrez JCH, Dedini FG. Gear shifting optimization applied to a flex-fuel vehicle under real driving conditions. Mech Based Des Struct Mach 2020;1–18. http://dx.doi.org/10.1080/15397734.2020.1769650.

[111] Lopes MV, Dias APC, Eckert JJ, dos Santos AA. Design of triple-beam internal-impact piezoelectric harvester optimized for energy and bandwidth. J Braz Soc Mech Sci Eng 2022. http://dx.doi.org/10.1007/s40430-022-03553-4.

[112] Roso VR, Martins MES. Simulation of fuel consumption and emissions for passenger cars and urban buses in real-world driving cycles. Tech. rep., SAE Technical Paper; 2016, http://dx.doi.org/10.4271/2016-36-0443.

[113] Roso VR, Santos NDSA, Valle RM, Alvarez CEC, Monsalve-Serrano J, García A. Evaluation of a stratified prechamber ignition concept for vehicular applications in real world and standardized driving cycles. Appl Energy 2019;254:113691. http://dx.doi.org/10.1016/j.apenergy.2019.113691.

[114] Berckmans G, Messagie M, Smekens J, Omar N, Vanhaverbeke L, Van Mierlo J. Cost projection of state of the art lithium-ion batteries for electric vehicles up to 2030. Energies 2017;10(9). http://dx.doi.org/10.3390/en10091314.

[115] Lutsey N, Nicholas M. Update on electric vehicle costs in the United States through 2030. Int Counc Clean Transp 2019;2.

[116] Fries M, Kerler M, Rohr S, Schickram S, Sinning M, et al. An overview of costs for vehicle components, fuels, greenhouse gas emissions and total cost of ownership update 2017 update. Technical report, 2018.

[117] Mongird K, Viswanathan VV, Balducci PJ, Alam MJE, Fotedar V, Koritarov VS, Hadjerioua B. Energy storage technology and cost characterization report. Tech. rep., Richland, WA (United States): Pacific Northwest National Lab.(PNNL); 2019.